Supporting Information

Ning et al. 10.1073/pnas.1401864111

SI Results and Discussion

The Effects of Disrupting the (D82)S13-(R111)L5 Interactions Predicted to Destabilize the Rotated-Subunit Orientation on PRE^{-A} Complex Dynamics. The $\Delta\Delta G_{L1}$ and $\Delta\Delta G_{L1\text{-tRNA}}$ values of $\sim$ +0.4 kcal·mol^{-1} that are observed for PRE$^{-A}_{(D82A)S13}$ and PRE$_{(D82K)S13}$ are smaller than the $\Delta\Delta G$ values that are typically observed when protein structures are destabilized by mutating charged amino acid residues involved in salt bridges to alanines ($\Delta\Delta G = 1$–5 kcal·mol^{-1}) (1). The attenuated effect of (D82)S13 mutations is likely due to the fact that (D82)S13 interacts with two oppositely charged amino acids in L5, (R111)L5 and (D112)L5, within the rotated (R)-subunit orientation, where the negatively charged oxygen atoms of the side-chain carboxyl groups of (D82)S13 are positioned such that they are slightly closer to the positively charged nitrogen atoms of the side-chain guanidinium groups of (R111)L5 (3.0 Å) than to the negatively charged oxygen atoms of the side-chain carboxyl groups of (D112)L5 (4.0 Å). We therefore speculate that, although (D82)S13 mutations disrupt the favorable electrostatic interactions between (D82)S13 and (R111)L5, they also alleviate the electrostatic repulsion between (D82)S13 and (D112)L5, thereby resulting in smaller values of $\Delta\Delta G$ than would normally be expected for the disruption of a salt bridge.

The Effects of Disrupting the (R3)S13–(D143)L5 Interactions Predicted to Destabilize the Nonrotated-Subunit Orientation on PRE^{-A} Complex Dynamics. Remarkably, the thermodynamic and kinetic effects conferred by disruption of the (R3)S13–(D143)L5 interactions in PRE$^{-A}_{(R3A)S13}$ and PRE$^{-A}_{(R3D)S13}$, relative to PRE$^{-A}_{(WT)S13}$, are almost identical to those conferred by completely deleting S13 in PRE$^{-A}_{(-)S13}$, relative to PRE$^{-A}_{(WT)S13}$ (Fig. 2 B, F, and G of the main text and Tables S2 and S3). This observation highlights the important role that the (R3)S13–(D143)L5 interaction plays in regulating the intersubunit, L1-stalk, and P-site tRNA dynamics of PRE/PRE^{-A} complexes and may provide an explanation for the extremely increased propensity of PRE complexes harboring (R3)S13 mutations to frameshift during translocation, the significantly decreased growth rate of *Escherichia coli* cells harboring (R3)S13 mutations, and the high degree to which this electrostatic intersubunit interaction is conserved in bacterial ribosomes (2).

Disruption of the (R3)S13–(D143)L5 Interaction Yields Small but Reproducible Decreases in $k_{L1c\rightarrow L1o}$ and $k_{L1\cdot tRNA\rightarrow L1o\cdot tRNA}$. Given that disruption of the (R3)S13–(D143)L5 interaction is predicted to destabilize the nonrotated (NR)-subunit orientation and consequently result in an increase in $k_{NR\rightarrow R}$, the observation that PRE$^{-A}_{(R3A)S13}$ and PRE$^{-A}_{(R3D)S13}$ exhibited two- to fivefold increases in $k_{L1o\rightarrow L1c}$ and $k_{L1o\cdot tRNA\rightarrow L1\cdot tRNA}$ is consistent with a model in which L1-stalk and P-site tRNA dynamics are coupled to intersubunit rotation in PRE/PRE^{-A} complexes. Nonetheless, in addition to the two- to fivefold increases in $k_{L1o\rightarrow L1c}$ and $k_{L1o\cdot tRNA\rightarrow L1\cdot tRNA}$, PRE$_{(R3A)S13}$ and PRE$_{(R3D)S13}$ also exhibited small, but detectable and reproducible, decreases in the rates of the reverse transitions (i.e., $k_{L1c\rightarrow L1o}$ and $k_{L1\cdot tRNA\rightarrow L1o\cdot tRNA}$) (Tables S2 and S3). There are at least two possible origins of these small effects (Fig. S3). The first possibility is that these small decreases in $k_{L1c\rightarrow L1o}$ and $k_{L1\cdot tRNA\rightarrow L1o\cdot tRNA}$ arise from an (R3)S13 mutation-mediated increase in the stability of the R-subunit orientation of the PRE^{-A} complexes. Although within the R-subunit orientation, (R3)S13 is too far away from any negatively charged residues within the 50S subunit to form salt bridges (see the structural analysis described in Fig. 1 of the main text), it is nonetheless likely that (R3)S13 participates in a network of relatively weaker,

longer-distance, electrostatic interactions with other charged residues within the PRE^{-A} complex. Given such a scenario, mutations to (R3)S13 could potentially alter this network in such a way to stabilize the R-subunit orientation of the PRE^{-A} complex, thus providing a plausible explanation for the small decreases in $k_{L1c\rightarrow L1o}$ and $k_{L1\cdot tRNA\rightarrow L1o\cdot tRNA}$ that we observe in PRE$^{-A}_{(R3A)S13}$ and PRE$^{-A}_{(R3D)S13}$. The second possibility is that our mutations to (R3)S13 alter the stability of one or more of the transition-state subunit orientations that are sampled during R→NR transitions in a manner that slightly increases the overall free-energy barrier that must be overcome for PRE/PRE^{-A} complexes to undergo R→NR transitions. Thus, within wild-type ribosomes, (R3)S13 not only stabilizes the NR-subunit orientation of the PRE complex, but also likely helps to establish the stability of the R-subunit orientation and/or the transition-state subunit orientations that are sampled during R→NR transitions.

(R3)S13–(D143)L5 and (D82)S13–(R111)L5 Interactions Act Independently to Regulate PRE Complex Dynamics. Having characterized the effects that disrupting either the (D82)S13–(R111)L5 interaction or the (R3)S13–(D143)L5 interaction have on intersubunit, L1-stalk, and tRNA dynamics, we next asked whether these interactions function independently or cooperatively to regulate intersubunit, L1-stalk, and tRNA dynamics in PRE complexes. To address this question, we investigated the thermodynamic and kinetic properties of PRE$^{-A}_{(R3D/D82K)S13}$, which harbors a (R3D/D82K)S13 double mutation. As shown in Fig. 2H of the main text and Tables S2 and S3, PRE$^{-A}_{(R3D/D82K)S13}$ exhibited two- to threefold increases in K_{L1} and $K_{L1\text{-tRNA}}$, corresponding to $\Delta\Delta G_{L1}$ and $\Delta\Delta G_{L1\text{-tRNA}}$ values of $\sim$ −0.6 kcal·mol^{-1} that favor the L1$_c$ and L1•tRNA conformations of the PRE^{-A} complexes. These equilibrium shifts were driven by three- to fourfold increases in $k_{L1o\rightarrow L1c}$ and $k_{L1o\cdot tRNA\rightarrow L1\cdot tRNA}$ and by twofold increases in $k_{L1c\rightarrow L1o}$ and $k_{L1\cdot tRNA\rightarrow L1o\cdot tRNA}$ (Tables S2 and S3). The fact that the thermodynamic and kinetic effects of the single amino acid mutations observed in PRE$^{-A}_{(D82K)S13}$ and PRE$^{-A}_{(R3D)S13}$ are essentially additive rather than multiplicative compared with the thermodynamic and kinetic effects of the double mutation observed for PRE$^{-A}_{(R3D/D82K)S13}$ (Tables S2 and S3) strongly suggests that, within wild-type ribosomes, (R3)S13–(D143)L5 and (D82)S13–(R111)L5 interactions largely act independently to regulate the intersubunit, L1-stalk, and tRNA dynamics of PRE complexes.

Comparative Structural Analysis Suggests a Structural Basis for the Cooperativity Between L1-Stalk Dynamics and Intersubunit Rotation. Analysis of X-ray crystallographic structures of ribosomal complexes in their NR- and R-subunit orientations (3–5) provides hints into the structural basis for the cooperativity that we observe between intersubunit rotation and L1-stalk dynamics (Fig. S5). In the R-subunit orientation, the L1$_c$ conformation of the L1 stalk can dock into a pocket that is formed within the platform region of the 30S subunit and make favorable electrostatic and van der Waals packing interactions with ribosomal proteins S7 and S11, including interactions between the phosphate backbones of adenine 2147 and guanine 2148 in helix 78 of the L1 stalk and a highly conserved, positively charged residue, arginine 142, in S7 [percentage of identity (PID) of a positively changed amino acid at position 142 in S7 is 99% in prokaryotes] (Table S1). It is likely that these interactions help to stabilize the L1$_c$ conformation of the L1 stalk within the context of the R-subunit orientation. In contrast, the relative geometry between the platform of the 30S subunit and the L1 stalk within the NR-

subunit orientation is such that, rather than being able to dock into the pocket formed by ribosomal proteins S7 and S11, the L1$_c$ conformation of the L1 stalk would instead sterically clash with ribosomal protein S11. It is likely that this steric clash precludes the L1 stalk from adopting the L1$_c$ conformation within the context of the NR-subunit orientation, thereby favoring the L1$_o$ conformation of the L1 stalk.

SI Materials and Methods

1. Phylogenetic Analyses of Ribosomal Proteins S7, S13, and L5. The sequences of ribosomal proteins S7, S13, and L5 were extracted from 971 fully sequenced genomes of phylogenetically diverse eubacterial and archaebacterial species as previously described (6). The sequences for each protein were aligned using Clustal Omega (7) and the alignments were visualized and analyzed using Jalview (8). The sequences of ribosomal proteins S7, S13, and L5 from *E. coli* K12 MG1655 were used as the reference sequences for the corresponding alignments. To extend our analysis, we compared the alignment of the 971 bacterial sequences described above to the alignment of the prokaryotic and eukaryotic sequences of the PFAM family members of ribosomal proteins S7 (PF00177, 5,281 sequences), S13 (PF00416, 4,002 sequences), and L5 (PF00673, 3,719 sequences) (9). PID values for several amino acids in these proteins are shown in Table S1.

2. Mutagenesis and Purification of Ribosomal Protein S13. The wild-type *E. coli rpsM* gene, which encodes ribosomal protein S13, was cloned from *E. coli* C600 genomic DNA into the pET26b(+) plasmid system (Novagen) under the control of an inducible T7 promoter. All S13 mutants, including (R3A)S13, (R3D)S13, (D82A)S13, (D82K)S13, and (R3D/D82K)S13, were constructed using the QuikChange Mutagenesis System (Stratagene) and, following the manufacturer's instructions, to introduce the mutation of interest into the pET26b(+) plasmid bearing the cloned, wild-type S13 gene. Proper introduction of the mutation of interest was verified by DNA sequencing. Wild-type S13 and all S13 mutants were overespressed in *E. coli* strain BL21(DE3) and purified using slight modifications of a previously published protocol (10). Briefly, cells containing overexpressed wild-type S13 or S13 mutants were disrupted using a French Press and the resulting cell lysate was dialyzed overnight at 4 °C, using 3,500 g·mol^{-1} molecular weight cutoff dialysis tubing and two changes of 1-L vol of protein purification (PP) buffer A [20 mM Tris(hydroxymethyl)amino-methane hydrochloride (Tris·HCl) (pH$_4$ $_{°C}$ 7.0), 20 mM potassium chloride (KCl), 6 M urea, and 6 mM β-mercaptoethanol (βME)] as a dialysis buffer. Using an AKTA Purifier Fast Protein Liquid Chromatography system (GE Lifesciences), the dialyzed cell lysate was loaded onto a HiTrap SP HP cation-exchange chromatography column that had been preequilibrated against PP buffer B [20 mM sodium acetate (NaOAc) (pH 5.6), 20 mM KCl, 6 M urea, and 6 mM βME)] and was eluted from the column using a 0–100% PP buffer C [20 mM NaOAc (pH 5.6), 1 M KCl, 6 M urea, and 6 mM βME] gradient that was applied over a gradient length of 20 column volumes. Protein-containing fractions were identified by Tris-tricine-SDS polyacrylamide gel electrophoresis and appropriate fractions were dialyzed against PP buffer D [80 mM potassium (4-(2-hydroxyethyl)-1-piperazineethanesulfonic acid) (K$^+$-Hepes) (pH 7.6), 20 mM magnesium chloride (MgCl$_2$), 1 M KCl, and 6 mM βME] and stored in PP buffer D at –80 °C until further use.

3. Preparation of 30S Subunits. Wild-type 30S subunits from *E. coli* K12 strain MG1655 cells were purified by sucrose density gradient ultracentrifugation, using a previously described protocol (11). The wild-type 30S subunits were stored in ribosome storage buffer [20 mM Tris(hydroxymethyl)aminomethane acetate (Tris-OAc) (pH$_4$ $_{°C}$ 7.5), 60 mM ammonium chloride (NH$_4$Cl),

0.5 mM EDTA, and 6 mM βME] containing 7.5 mM magnesium acetate [Mg(OAc)$_2$] at –80 °C. The 30S subunits lacking S13 [(–)S13] were purified from strain MG1655-derived cells from which the *rpsM* gene encoding S13 had been deleted (a kind gift of strain S13MG1 from Rachel Green, Johns Hopkins University School of Medicine) (2). (–)S13 30S subunits were purified using the same procedure that was used to purify wild-type 30S subunits with the only difference being that the Mg^{2+} concentration at all steps of the purification was raised to 20 mM. The only exception was the step of the purification in which sucrose density gradient ultracentrifugation was used to dissociate the 70S ribosomes into 30S and 50S subunits; the Mg^{2+} concentrations of the buffer that was used to prepare the sucrose solutions for this step were maintained at 1 mM to allow effective dissociation of the 70S ribosomes into 30S and 50S subunits. (–)S13 30S subunits were stored in ribosome storage buffer containing 20 mM Mg(OAc)$_2$.

S13 reconstitution reactions were used to reconstitute wild-type S13 or each S13 mutant into (–)S13 30S subunits, using a previously published protocol (Fig. S2) (2). S13 reconstitution reactions were prepared by mixing 1.2 nmol of (–)S13 30S subunits in ribosome storage buffer containing 20 mM Mg(OAc)$_2$ with a sixfold excess of wild-type S13 or S13 mutant in PP buffer D (or just PP buffer D, as a negative control) and diluting the reaction with enough reconstitution buffer [80 mM K$^+$-Hepes (pH 7.6), 20 mM MgCl$_2$, 330 mM KCl, and 0.01% octaethylene glycol monon-dodecyl ether] (Nikkol; Calbiochem) to yield final concentrations of 1.6 μM (–)S13 30S subunits and 10 μM wild-type S13 (or S13 mutant). S13 reconstitution reactions were incubated for 1 h at 42 °C and S13-reconstituted 30S subunits were purified away from (–)S13 30S subunits, using a previously published subunit association-based purification protocol (2). Briefly, subunit association reactions were prepared by adding 1.2 nmol of wild-type 50S subunits in ribosome storage buffer containing 7.5 mM Mg(OAc)$_2$ (*SI Materials and Methods*, section 4) to each S13 reconstitution reaction and then diluting the resulting mixture with subunit association buffer [50 mM Tris·HCl (pH 7.5), 70 mM NH$_4$Cl, 30 mM KCl, 15 mM MgCl$_2$] to yield final concentrations of 0.8 μM (–)S13 30S subunits and 0.8 μM wild-type 50S subunits. Subunit association reactions were incubated at 37 °C for 1 h, were loaded onto 10–40% (wt/vol) sucrose concentration gradients prepared in subunit association buffer, were centrifuged for 17 h at 22,000 rpm using an SW28 rotor in a Beckman Optima L70 Ultracentrifuge, and were analyzed as described previously (12). As expected from previous studies (2), control subunit association reactions performed using S13 reconstitution reactions that lacked wild-type S13 or S13 mutants (i.e., reconstitution reactions performed using PP buffer D rather than wild-type S13 or S13 mutants) resulted in (–)S13 30S subunits that failed to associate with wild-type 50S subunits and form 70S ribosomes (Fig. S2*B*). In contrast, subunit association reactions performed using S13 reconstitution reactions that contained either wild-type S13 or S13 mutants resulted in S13-reconstitiuted 30S subunits that successfully associated with wild-type 50S subunits and formed 70S ribosomes (Fig. S2*C*). Thus, the 70S ribosome peak in the sucrose density gradient profile shown in Fig. S2*C* should contain 70S ribosomes that are composed exclusively of S13-reconstituted 30S subunits and wild-type 50S subunits. Preparative sucrose density gradient ultra-centrifugation of subunit association reactions performed using S13 reconstitution reactions containing either wild-type S13 or each S13 mutant therefore allowed for purification of 70S ribosomes containing each S13-reconstitiued 30S subunit. S13-reconstituted 30S subunits were subsequently isolated by loading purified 70S ribosomes containing each S13-reconstitiued 30S subunit onto a 10–40% (wt/vol) sucrose concentration gradient prepared in subunit dissociation buffer [50 mM Tris·HCl (pH 7.5), 70 mM NH$_4$Cl, 30 mM KCl, 1 mM MgCl$_2$] and centrifuging for

17 h at 22,000 rpm, using an SW28 rotor in a Beckman Optima L70 Ultracentrifuge to separate and purify S13-reconstituted 30S subunits away from the wild-type 50S subunits. S13-reconstituted 30S subunits were stored in ribosome storage buffer containing 20 mM Mg(OAc)$_2$. Comparing the area underneath the 70S ribosome peak in the sucrose density gradient profile obtained in the absence of wild-type S13 or S13 mutants (Fig. S2*B*) with that obtained in the presence of wild-type S13 or each S13 mutant (Fig. S2*C*) revealed that all S13-reconstituted 30S subunits were >98% pure and contained <2% contaminating (−)S13 30S subunits.

4. Preparation of 50S Subunits. Wild-type 50S subunits from *E. coli* K12 strain MG1655 cells were purified by sucrose density gradient ultracentrifugation, using a previously described purification protocol (11), and stored in ribosome storage buffer containing 7.5 mM Mg(OAc)$_2$.

The 50S subunits containing Cy3-labeled L9 and Cy5-labeled L1 and 50S subunits containing Cy5-labeled L1 were prepared as previously described (13, 14). Briefly, 50S subunits containing Cy3-labeled L9 and Cy5-labeled L1 were prepared by (*i*) purifying 50S subunits lacking L9 and L1, using sucrose density gradient ultracentrifugation of 50S subunits from an *E. coli* BW25113-based strain in which the genes encoding L9 (*rplI*) and L1 (*rplA*) have been deleted; (*ii*) purifying recombinantly expressed, single-cysteine, six-histidine affinity-tagged mutants of L9 [L9(Q18C)] and L1 [L1(T202C)], using nickel nitrilotriacetic acid (Ni^{2+}-NTA) affinity chromatography; (*iii*) proteolytically removing the six-histidine affinity tag from L9(Q18C) and L1(T202C); (*iv*) labeling L9(Q18C) and L1(T202C) with maleimide-derivatized Cy3 and Cy5 fluorophores (GE Lifesciences), respectively; (*v*) purifying the resulting Cy3-labeled L9(Q18C) and Cy5-labeled L1(T202C), using a Superdex 75 gel filtration column on an Fast Protein Liquid Chromatography system (AKTA Purifier; GE Lifesciences); (*vi*) reconstituting Cy3-labeled L9(Q18C) and Cy5-labeled L1(T202C) into the 50S subunits lacking L1 and L9; and (*vii*) purifying 50S subunits reconstituted with Cy3-labeled L9(Q18C) and Cy5-labeled L1(T202C) away from unincorporated Cy3-labeled L9(Q18C) and Cy5-labeled L1(T202C), using sucrose density gradient ultracentrifugation (13). The 50S subunits containing Cy5-labeled L1 were prepared in a manner similar to that in which 50S subunits containing Cy3-labeled L9 and Cy5-labeled L1 were prepared, with the exception that purified, Cy5-labeled L1(T202C) was reconstituted into 50S subunits lacking L1 that had been purified from an *E. coli* BW25113-based strain in which only the gene encoding L1 (*rplA*) had been deleted using sucrose density gradient ultracentrifugation (14).

5. Preparation of mRNAs, tRNAs, and Translation Factors. mRNA templates were in vitro transcribed using T7 RNA polymerase from double-stranded DNA templates encoding variants of the bacteriophage T4 gene product 32 and purified using a protocol described previously (12). For the EF-G–independent translocation assays (*SI Materials and Methods*, sections 8 and 9), a truncated T4 gene product 32 mRNA encoding the first 20 aa (hereafter referred to as T4gp32$_{1–20}$) was used. The first three codons of the T4gp32$_{1–20}$ mRNA are AUG–UUU–AAA, encoding an fMet–Phe–Lys tripeptide). The mRNA used for the single-molecule fluorescence resonance energy transfer (smFRET) experiments has been previously described [mRNA (tRNA^{Phe}) in figure S1 of ref. 15] and was prepared as previously described (16). Briefly, a 3′-biotinylated DNA oligonucleotide (TGTGTAAGTTTTAGGTTGATTTG-Biotin; Integrated DNA Technologies) was hybridized to mRNA(tRNA^{Phe}) to enable tethering of PRE$^{−A}$ complexes to the surface of the microfluidic flow cells that are used for total internal reflection fluorescence (TIRF) microscopy as previously described (12). In mRNA (tRNA^{Phe}), the usual AUG start codon has been mutagenized to a UUC codon, thus enabling a deacylated tRNA^{Phe} to be non-enzymatically loaded into the ribosomal P site during non-enzymatic preparation of PRE$^{−A}$ complexes (*SI Materials and Methods*, section 6). Hereafter, we use the term "biotin–mRNA" to refer to the DNA–mRNA hybrid that is generated by hybridizing the 3′-biotinylated DNA oligonucleotide to mRNA(tRNA^{Phe}).

All tRNAs used in this study were from *E. coli* and were purchased from either Sigma (tRNA^{Phe}) or MP Biomedicals (tRNA^{fMet} and tRNA^{Lys}). Cy3-labeled tRNA^{Phe} was prepared by using *N*-hydroxysuccinimidyl ester-derivatized Cy3 fluorophore (GE Lifesciences) to label the 3-(3-amino-3-carboxy-propyl) uridine 47 position of tRNA^{Phe} and the resulting Cy3-labeled tRNA^{Phe} was purified away from non–Cy3-labeled tRNA^{Phe} using hydrophobic interaction chromatography as previously described (11). Previously published procedures were used to aminoacylate (with either [^{35}S]-methionine or nonradioactively labeled methionine) and formylate tRNA^{fMet}, aminoacylate tRNA^{Phe} and tRNA^{Lys}, and purify formylated and/or aminoacylated tRNAs away from nonformylated and/or nonacylated tRNAs (12).

Initiation factor (IF)1, IF2, and IF3 and elongation factor (EF)-Tu, EF-Ts, and EF-G were overexpressed, purified, and stored as previously described (11, 12).

6. Assembly and Purification of PRE$^{−A}$ Complexes and Vacant 70S Ribosomes. PRE$^{−A}$ complexes, rather than PRE complexes, were used for the smFRET studies reported here to avoid the heterogeneity that arises from differences in the presence, absence, and acylation status of an aminoacyl–tRNA binding (A)-site peptidyl–tRNA in PRE complexes (11, 13, 14) and the heterogeneity that arises from the EF-G–independent translocation of PRE complexes lacking S13 and possibly of PRE complexes harboring S13 mutants (2). There is precedence for such an approach in that PRE$^{−A}$ complexes are routinely used as models of PRE complexes in biochemical, structural, and smFRET studies of translocation (5, 16).

PRE$^{−A}$ complexes for smFRET experiments were assembled in a two-step reaction as previously described (16). In the first step, a mixture of biotin–mRNA, either nonaminoacylated Cy3-labeled tRNA^{Phe} (for PRE$^{−A}$ complexes for smFRET$_{L1-tRNA}$ experiments) or nonaminoacylated non–Cy3-labeled tRNA^{Phe} (for PRE$^{−A}$ complexes for smFRET$_{L1–L9}$ experiments) and either wild-type 30S subunits or the appropriate S13-reconstituted 30S subunits, was incubated for 10 min at 37 °C in PRE$^{−A}$ assembly buffer [50 mM Tris·HCl (pH$_{25\ °C}$ 7.5), 70 mM NH$_4$Cl, 30 mM KCl, and 6 mM βME] containing 7 mM MgCl$_2$. In the second step, either 50S subunits containing Cy5-labeled L1 (for PRE$^{−A}$ complexes for smFRET$_{L1-tRNA}$ experiments) or 50S subunits containing Cy3-labeled L9 and Cy5-labeled L1 (for PRE$^{−A}$ complexes for smFRET$_{L1–L9}$ experiments) were added to each mixture from the first step and the resulting reactions were incubated for an additional 20 min at 37 °C. The final concentrations of all components in each of these PRE$^{−A}$ complex formation reactions were 0.3 μM biotin–mRNA, 0.2 μM tRNA^{Phe}, 0.15 μM 30S subunits, and 0.1 μM 50S subunits in ∼30 μL.

Vacant 70S ribosomes for smFRET$_{L1–L9}$ experiments were assembled in a manner identical to that described for the assembly of PRE$^{−A}$ complexes for smFRET$_{L1–L9}$ experiments with two exceptions. The first exception was that tRNA^{Phe} was not included in the first step of the PRE$^{−A}$ complex formation reaction. The second exception was that the reaction was performed in PRE$^{−A}$ assembly buffer containing 20 mM MgCl$_2$ [we have found that 70S ribosomes containing (−)S13 30S subunits can be successfully formed and subsequently purified using sucrose density gradient ultracentrifugation when the concentration of Mg^{2+} in PRE$^{−A}$ assembly buffer is 20 mM]. The volumes of all PRE$^{−A}$ and vacant 70S ribosome formation reactions were ad-

justed to 100 µL with Tris-Polymix buffer [50 mM Tris-OAc (pH$_{25 \,°C}$ 7.0), 100 mM KCl, 5 mM ammonium acetate (NH$_4$OAc), 0.5 mM calcium acetate [Ca(OAc)$_2$], 0.1 mM EDTA, 10 mM βME, 5 mM putrescine dihydrochloride (putrescine-HCl), and 1 mM spermidine, free base] containing 20 mM Mg(OAc)$_2$ and were subsequently layered onto a 10–40% (wt/vol) sucrose concentration gradient prepared in Tris-Polymix buffer containing 20 mM Mg(OAc)$_2$ and purified using sucrose density gradient ultracentrifugation by centrifuging for 12 h at 25,000 rpm, using an SW41 rotor in a Beckman Optima L70 Ultracentrifuge as previously described (11, 14).

7. Assembly and Purification of PRE Complexes. PRE complexes for EF-G–independent translocation assays were prepared in a three-step reaction, using a modified version of a previously published protocol (2). In the first step, a 70S ribosomal initiation complex (70S IC) was formed by incubating IF1, IF2, IF3, GTP, either wild-type 30S subunits or the appropriate S13-reconstituted 30S subunits, and wild-type 50S subunits for 10 min at 37 °C in translocation buffer [50 mM Tris·HCl (pH$_{25 \,°C}$ 7.5), 70 mM NH$_4$Cl, 30 mM KCl, 1 mM DTT, and 7 mM MgCl$_2$]; adding T4gp32$_{1–20}$ mRNA and incubating for an additional 10 min at 37 °C; and adding f-[^{35}S]Met-tRNA^{fMet} and incubating for an additional 10 min at 37 °C. The final concentrations of all components in each of these 70S IC formation reactions were 1.2 µM IF1, 1.2 µM IF2, 1.2 µM IF3, 0.8 mM GTP, 0.8 µM 30S subunits, 0.8 µM unlabeled 50S subunits, 0.4 µM f-[^{35}S]Met-tRNA^{fMet}, and 1.6 µM T4gp32$_{1–20}$ mRNA in ~10 µL. In the second step, a ternary complex composed of EF-Tu, GTP, and Phe-tRNA^{Phe} [EF-Tu(GTP)Phe-tRNA^{Phe}] was prepared by incubating EF-Tu, EF-Ts, GTP, phosphoenolpyruvate, and pyruvate kinase (Sigma) in translocation buffer for 1 min at 37 °C and for an additional 1 min on ice; adding Phe-tRNA^{Phe} and incubating for an additional 1 min at 37 °C; and storing the resulting EF-Tu(GTP)Phe-tRNA^{Phe} on ice until use. The final concentrations of all components in this EF-Tu(GTP)Phe-tRNA^{Phe} formation reaction were 20 µM EF-Tu, 13.4 µM EF-Ts, 0.5 mM GTP, 3 mM phosphoenolpyruvate, 1 unit·mL$^{−1}$ pyruvate kinase, and 2 µM Phe-tRNA^{Phe} in ~10 µL. In the third step, 6 µL of EF-Tu(GTP)Phe-tRNA^{Phe} formation reaction and 1.5 µL of translocation buffer were added to 7.5 µL of each 70S IC formation reaction and the resulting PRE complex formation reaction was incubated for 5 min at room temperature.

8. EF-G–Independent Translocation Assays. To investigate whether the stabilities of the PRE-complex conformation that is compatible with translocation (i.e., in which the conformational equilibria of the PRE complex are shifted toward L1$_c$ and L1●tRNA) or the PRE-complex conformation that is incompatible with translocation (i.e., in which the conformational equilibria of the PRE complex are shifted toward L1$_o$ and L1∘tRNA) correlate with the propensity of PRE complexes to undergo EF-G–independent translocation, we used two independent biochemical assays (Fig. S6), a puromycin reactivity assay and a tripeptide synthesis assay, to quantify the EF-G–independent translocation activities of PRE complexes that were analogous to a subset of the PRE$^{−A}$ complexes used in our smFRET experiments. Because the smFRET experiments were conducted in Tris-Polymix buffer containing 15 mM Mg^{2+} and the EF-G–independent translocation assays had to be conducted in translocation buffer containing 8 mM Mg^{2+} to achieve reliably quantifiable levels of EF-G–independent translocation, we began by repeating the smFRET$_{L1-tRNA}$ experiments on three PRE$^{−A}$ complexes [PRE$^{−A}_{(WT)S13}$, PRE$^{−A}_{(D82K)S13}$, and PRE$^{−A}_{(R3D)S13}$] in translocation buffer containing 8 mM Mg^{2+} to ensure that the effects of the D82K and R3D S13 mutations on the L1∘tRNA⇌L1●tRNA equilibrium were not dependent on the concentration of Mg^{2+} in the two different buffers. Indeed, the results of these smFRET experiments revealed that,

relative to PRE$^{−A}_{(WT)S13}$, PRE$^{−A}_{(D82K)S13}$ and PRE$^{−A}_{(R3D)S13}$ exhibit shifts of the L1∘tRNA⇌L1●tRNA equilibrium in translocation buffer containing 8 mM Mg^{2+} that are similar to those observed in Tris-Polymix buffer containing 15 mM Mg^{2+} (Fig. S6A).

Because previous studies have used a puromycin reactivity assay to assess the rate and extent of EF-G–independent translocation of PRE complexes containing S13-reconstituted 30S subunits (2), we began by using a slightly modified version of this previously published puromycin reactivity assay to assess the rate and extent of EF-G–independent translocation in our PRE complexes (17). Briefly, puromycin reactions were prepared by adding 1 µL of 10 mM puromycin prepared in translocation buffer added to 9 µL of PRE-complex formation reactions prepared as described in *SI Materials and Methods*, section 7. The puromycin solutions and PRE-complex samples were preincubated for 3 min at 37 °C before mixing. After mixing, the puromycin reactions were incubated at 37 °C and 1-µL aliquots were collected at the specified time points. It should be noted that, because the ribosome storage buffer in which the 30S and 50S subunits were stored contains 20 mM and 7.5 mM Mg (OAc)$_2$, respectively, the final concentration of Mg^{2+} in the puromycin reactions was ~8 mM. Immediately upon the collection of each aliquot at each time point, the puromycin reaction was quenched by the addition of 1 µL of 1 M potassium hydroxide (KOH) to each aliquot, thereby releasing any unreacted fMet amino acid from tRNA^{fMet} and any unreacted fMet–Phe dipeptide from tRNA^{Phe}. The unreacted fMet amino acid, unreacted fMet–Phe dipeptide, and fMet–Phe–Pm product (where Pm denotes puromycin) were resolved using electrophoretic TLC (eTLC) as previously described (17). eTLC plates were exposed to a PhosphorImager screen (GE Lifesciences), the screen was scanned with a Typhoon FLA 7000 PhosphorImager (GE Lifesciences), and spots were quantified using ImageQuant (Molecular Dynamics) software. The fraction of fMet–Phe–Pm at each time point was calculated as

$$\%_{\text{Di–Pm}} = \frac{I_{\text{Di-Pm}}}{I_{\text{Di-Pm}} + I_{\text{Di}}} \times 100\%,$$

where $\%_{\text{Di-Pm}}$ is the fraction fMet–Phe–Pm, $I_{\text{Di-Pm}}$ is the intensity of the spot corresponding to fMet–Phe–Pm, and I_{Di} is the intensity of the spot corresponding to fMet–Phe (Fig. S6 *B* and *C*).

Assessing the rate and extent of EF-G–independent translocation using puromycin reactivity assays is complicated by the fact that both the fMet–Phe dipeptide from the P/P-configured peptidyl-tRNA in the P site of the ribosomal posttranslocation complex (18) and the fMet–Phe dipeptide from the A/P-configured peptidyl-tRNA in the A site of the ribosomal pretranslocation (i.e., PRE) complex (19) can react with puromycin and form fMet–Phe–Pm. To eliminate this complication, we independently assessed the rate and extent of EF-G–independent translocation, using a tripeptide synthesis assay (Fig. S6 *D* and *E*) such that only the fMet–Phe dipeptide from the P/P-configured peptidyl-tRNA in the P site of the ribosomal posttranslocation complex would be capable of reacting with a third aa-tRNA (i.e., Lys-tRNA^{Lys}) to form a tripeptide product. Tripeptide synthesis reactions were performed using a slightly modified version of a previously published three-step reaction protocol (17). In the first step, 70S IC formation reactions containing either wild-type 30S subunits or the appropriate S13-reconstituted 30S subunits were prepared as described in *SI Materials and Methods*, section 7. In the second step, a mixture of EF-Tu(GTP)Phe-tRNA^{Phe} and EF-Tu(GTP)Lys-tRNA^{Lys} ternary complexes was prepared by incubating EF-Tu, EF-Ts, GTP, phosphoenolpyruvate, and pyruvate kinase (Sigma) in translocation buffer for 1 min at 37 °C and for an additional 1 min on ice; adding Phe-tRNA^{Phe} and Lys-

tRNA^{Lys} and incubating for an additional 1 min at 37 °C; and storing the resulting EF-Tu(GTP)Phe-tRNA^{Phe} and EF-Tu(GTP) Lys-tRNA^{Lys} mixture on ice until use. The final concentrations of all components in this EF-Tu(GTP)Phe-tRNA^{Phe} and EF-Tu(GTP)Lys-tRNA^{Lys} formation reaction were 20 μM EF-Tu, 13.4 μM EF-Ts, 0.5 mM GTP, 3 mM phosphoenolpyruvate, 1 unit·mL^{-1} pyruvate kinase, 2 μM Phe-tRNA^{Phe}, and 2 μM Lys-tRNA^{Lys} in ~10 μL. In the third step, tripeptide synthesis reactions were prepared by adding 6 μL of EF-Tu(GTP)Phe-tRNA^{Phe} and EF-Tu(GTP)Lys-tRNA^{Lys} formation reaction and 1.5 μL of translocation buffer to 7.5 μL of each 70S IC formation reaction. Tripeptide synthesis reactions were first incubated at room temperature for 5 min and were transferred to a 37 °C heat block, and 1-μL aliquots were collected at the specified time points. The tripeptide synthesis reaction in each aliquot at each time point was quenched with 1 M KOH as described above for the puromycin reactivity assays and the reaction products were separated by eTLC, visualized by Phosphor-Imaging, and quantified as described above for the puromycin reactivity assays, with the exception that the equation that was used for quantification was

$$\%_{Tri} = \frac{I_{Tri}}{I_{Tri} + I_{Di}} \times 100\%,$$

where $\%_{Tri}$ is the fraction fMet–Phe–Lys, I_{Tri} is the intensity of the spot corresponding to fMet–Phe–Lys, and I_{Di} is the intensity of the spot corresponding to fMet–Phe (Fig. S6 *D* and *E*).

9. Mg^{2+} Dependence of PRE Complex Dynamics and EF-G–Independent Translocation. Previous studies have demonstrated that Mg^{2+} concentration is an effective regulator of the classical⇋hybrid, L1$_o$⇋L1$_c$, and L1∘tRNA⇋L1•tRNA equilibria within PRE^{-A} and PRE complexes, with decreasing Mg^{2+} concentrations shifting these equilibria toward the hybrid P/deacylated (or exit) tRNA binding (P/E) and A/P tRNA configurations, the L1$_c$ conformation of the L1 stalk, and a direct physical contact between the closed L1 stalk and the P/E-configured tRNA in the P site of the PRE complex (L1•tRNA) (20, 21). Thus, the conformation of the PRE complex that is stabilized at low Mg^{2+} concentrations is expected to be similar to or the same as that of the PRE complex conformation that is described in *SI Materials and Methods*, section 8 as being compatible with translocation. Therefore, to provide further evidence to support our finding that the PRE-complex conformation exhibiting hybrid P/E and A/P tRNA configurations, the L1$_c$ conformation of the L1 stalk, and a direct physical contact between the closed L1 stalk and the P/E-configured tRNA in the P site of the PRE complex (L1•tRNA) promotes the EF-G–independent translocation, we performed tripeptide synthesis assays to assess the rate and extent of EF-G–independent translocation as a function of Mg^{2+} concentration. These experiments were performed using PRE$_{(R3D)S13}$, the PRE complex that shows the fastest rate and greatest extent of EF-G–independent translocation. The experimental protocol was similar to that used to perform the tripeptide synthesis assays described in *SI Materials and Methods*, section 8 above with the exception that, after the tripeptide synthesis reaction was initiated by adding 14.4 μL of EF-Tu(GTP)Phe-tRNA^{Phe} and EF-Tu(GTP)Lys-tRNA^{Lys} formation reaction to 18 μL of 70S IC formation reaction, the resulting tripeptide synthesis reaction was separated into four aliquots of ~8 μL each (at ~8 mM Mg^{2+} each, initially) and the Mg^{2+} concentration was adjusted to 8 mM, 10 mM, 12 mM, and 15 mM by the addition of 0.8 μL of translocation buffer that had been adjusted to 8 mM, 28 mM, 48 mM, and 78 mM MgCl$_2$, respectively. Tripeptide synthesis reactions were first incubated at room temperature for 5 min and were transferred to a 37 °C heat block, and 1-μL aliquots were collected at the specified

time points. The tripeptide synthesis reaction in each aliquot at each time point was quenched with 1 M KOH as described in *SI Materials and Methods*, section 8 above for the tripeptide synthesis reactions and the reaction products were separated by eTLC, visualized by PhosphorImaging, and quantified as described in the *SI Materials and Methods*, section 8 above for the tripeptide synthesis reactions. Consistent with our finding that that the PRE-complex conformation exhibiting hybrid P/E and A/P tRNA configurations, the L1$_c$ conformation of the L1 stalk, and a direct physical contact between the closed L1 stalk and the P/E-configured tRNA in the P site of the PRE complex (L1•tRNA) promotes EF-G–independent translocation, the results of our Mg^{2+} titration experiments demonstrated that decreasing concentrations of Mg^{2+}, which favors the hybrid P/E and A/P tRNA configurations, the L1$_c$ conformation of the L1 stalk, and a direct physical contact between the closed L1 stalk and the P/E-configured tRNA in the P site of the PRE complex (L1•tRNA) (20, 21), also increases the rate and extent of EF-G–independent translocation of PRE$_{(R3D)S13}$ (Fig. S6*F*).

10. smFRET Imaging Using TIRF Microscopy. All smFRET experiments were performed in Tris-Polymix buffer containing 15 mM Mg(OAc)$_2$ and supplemented with an oxygen-scavenging system [protocatechuic acid (PCA)/protocatechuate-3,4-dioxygenase (PCD)] (15) and a triplet-state quencher mixture [1 mM 1,3,5,7-cyclooctatetraene (Sigma-Aldrich) and 1 mM 3-nitrobenzyl alcohol (Fluka)] (22) as previously described (13, 14, 16). Briefly, smFRET experiments were performed using a laboratory-built, prism-based TIRF microscope that uses a 532-nm diode-pumped solid-state laser (CrystaLaser) to directly excite Cy3, a 1.2-NA 60× water-immersion objective (PlanApo; Nikon) to collect the fluorescence emission from Cy3 and Cy5, a Dual-View multichannel imaging system (Photometrics) to wavelength separate the Cy3 and Cy5 signals, and a 512 × 512-pixel electron-multiplying charge-coupled-device (EMCCD) camera (Cascade II; Photometerics) to record the wavelength-separated Cy3 and Cy5 signals as a function of time (11, 14). This experimental setup allows simultaneous acquisition of both the Cy3 and Cy5 channels of a single field of view onto two halves of a single exposure of the EMCCD camera. For smFRET$_{L1–L9}$ experiments, the 532-nm laser was used at a laser power of 12 mW (measured just before the laser striking the prism) and the EMCCD camera was used at a time resolution of 10 frames·s^{-1} whereas for the smFRET$_{L1-tRNA}$ experiments, the 532-nm laser was used at a laser power of 16 mW (measured just before the laser striking the prism) and the EMCCD camera was used at a time resolution of 20 frames·s^{-1}. These laser power settings and EMCCD camera time resolutions for the two types of smFRET experiments allowed us to directly compare the smFRET data reported here with previously reported data from our laboratory (13, 14, 16). With the exception of 70S$_{(-)S13}$, this experimental setup enables us to record movies in which we capture ~200–300 spatially resolved PRE^{-A} complexes or vacant 70S ribosomes, within a field of view of 60 μm × 120 μm. In the case of 70S$_{(-)S13}$, we note that, despite the relatively weak association between (−)S13 30S and 50S subunits in the presence of subunit association buffer (*SI Materials and Methods*, section 4), we were still able to image ~100–200 vacant 70S$_{(-)S13}$ ribosomes within the field of view in the presence of Tris-Polymix buffer containing 15 mM Mg(OAc)$_2$ and supplemented with our oxygen-scavenging system and triplet-state quencher mixture. Presumably this is due to the stabilization of the interactions between the (−)S13 30S and 50S subunits in 70S$_{(-)S13}$ that is brought about by the 6-mM concentration of positively charged polyamines (5 mM putrescine-HCl and 1 mM spermidine, free base) in the Tris-Polymix buffer that is lacking in the subunit association buffer. To ensure that the majority of fluorophores photobleached within the ex-

perimental observation period, each field of view was imaged for an observation period of >60 s. Three independent datasets consisting of approximately three to eight fields of view each were collected for each PRE^{-A} complex or vacant 70S ribosome and the results of all analyzed parameters (i.e., FRET efficiencies, equilibrium constants, changes in free-energy differences, transition rates, etc.) for each PRE^{-A} complex or vacant 70S ribosome were reported as the mean and the SD based on these three independent datasets.

11. Identification of Single Cy3–Cy5 Fluorophore Pairs and Idealization of Single E_{FRET} vs. Time Trajectories. Identification of individual Cy3–Cy5 fluorophore pairs and idealization of the corresponding raw smFRET vs. time trajectories were performed as previously described (13, 14, 16) and are only briefly described here. Given the magnification of our TIRF microscope and the dimensions of the pixels in our EMCCD camera, the emission from a spatially well-resolved, single fluorophore is not expected to occupy a region greater than 2 × 2 neighboring pixels. Thus, spatially well-resolved, single Cy5 fluorophores in each movie were identified by (i) using the MetaMorph software suite (Molecular Devices) to compile a single image of the Cy5 half of the EMCCD camera in which each pixel of the compiled image contained the maximum Cy5 intensity ($I_{Cy5,max}$) of the corresponding pixel across all but the first 20 frames of the movie; (ii) generating a histogram of the intensities from all of the pixels in the image of $I_{Cy5,max}$; (iii) using the histogram to obtain an initial estimate of an intensity threshold that could be applied to the pixels in the image of $I_{Cy5,max}$ to identify pixels reporting on signals arising from Cy5 fluorophores (i.e., pixels with an $I_{Cy5,max}$ greater than the intensity threshold value) from pixels reporting on background noise (i.e., pixels with an $I_{Cy5,max}$ less than the intensity threshold); (iv) empirically optimizing the value of the intensity threshold such that when the intensity threshold is applied, >80% of the Cy5 fluorophores with an $I_{Cy5,max}$ greater than the intensity threshold occupy a region that is ≤2 × 2 neighboring pixels; (v) applying this optimized intensity threshold and the ≤2 × 2 neighboring pixel clustering criterion to the pixels in the image of $I_{Cy5,max}$ to identify ≤2 × 2 neighboring pixel clusters reporting on signals arising from single Cy5 fluorophores (i.e., clusters of ≤2 × 2 neighboring pixels with an $I_{Cy5,max}$ greater than the intensity threshold value) from signals arising from multiple Cy5 fluorophores (i.e., clusters of >2 × 2 neighboring pixels with an $I_{Cy5,max}$ greater than the intensity threshold value) and from pixels reporting on background noise (i.e., pixels with an $I_{Cy5,max}$ less than the intensity threshold); and (vi) combining the clusters of ≤2 × 2 neighboring pixels reporting on signals arising from single Cy5 fluorophores into regions defining single Cy5 fluorophores. Exclusion of the first 20 frames of each movie from the image of $I_{Cy5,max}$ ensured that only single Cy5 fluorophores with lifetimes >2 s for the smFRET$_{L1–L9}$ data and >1 s for the smFRET$_{L1-tRNA}$ data were identified by the intensity threshold analysis. The single Cy3 fluorophore corresponding to each selected single Cy5 fluorophore was then identified by transferring the coordinates of the regions corresponding to single Cy5 flurophores from the image of $I_{Cy5,max}$ to the corresponding coordinates of an analogous image of maximum Cy3 intensities from the Cy3 half of the EMCCD camera ($I_{Cy3,max}$) and defining regions corresponding to single Cy3 fluorophores by optimizing the alignment of the Cy5-defined regions within the image of $I_{Cy3,max}$ by visual inspection, thus defining the set of individual Cy3–Cy5 fluorophore pairs for each movie.

Transfer of the coordinates of the regions corresponding to individual Cy3–Cy5 fluorophore pairs from the images of $I_{Cy3,max}$ and $I_{Cy5,max}$ to each frame of the movie subsequently allowed Cy3–Cy5 intensity vs. time trajectories to be plotted for the entire set of individual Cy3–Cy5 fluorophore pairs (Fig. S1 A and B). Cy3–Cy5 intensity trajectories exhibiting single-step photo-

bleaching events were identified by visual inspection and were selected for further processing and analysis. Due to imperfect performance of the 680 ± 25-nm Cy5 emission filter, the Cy5 intensity at each time point of each Cy3–Cy5 intensity trajectory was bleedthrough corrected by subtracting 7% of the Cy3 intensity of the corresponding time point and, subsequently, each Cy3–Cy5 intensity trajectory was baseline corrected such that postphotobleaching Cy3 and Cy5 intensities average to zero intensity. Individual raw smFRET vs. time trajectories were plotted by calculating the FRET efficiency (E_{FRET}) at each time point, using $E_{FRET} = I_{Cy5}/(I_{Cy3} + I_{Cy5})$, where I_{Cy3} and I_{Cy5} are the Cy3 and Cy5 emission intensities at the corresponding time point, respectively (Fig. S1 A and B). Raw smFRET trajectories were then idealized using a hidden Markov model implemented using the vbFRET software program, which employs a maximum evidence-based model-selection algorithm that minimizes overfitting of the smFRET data and enables a more accurate determination of the number of FRET states present in each trajectory relative to more conventional, maximum likelihood-based model-selection algorithms (23). The maximum number of FRET states that vbFRET could attempt to fit was set to 5, and the number of fitting attempts to be made per smFRET trajectory was set to 25. Transitions in the idealized smFRET trajectories occurring between FRET states that were separated by less than $E_{FRET} = 0.05$ for smFRET$_{L1–L9}$ trajectories and $E_{FRET} = 0.1$ for smFRET$_{L1-tRNA}$ trajectories were discarded (<1% of the total transitions identified by vbFRET), because such transitions cannot be confidently distinguished from noise. Consistent with previously reported results (13, 16), vbFRET finds that a two-state model provides the maximum evidence and is therefore the model that is best supported by both smFRET$_{L1–L9}$ and smFRET$_{L1-tRNA}$ data.

12. Calculation of Equilibrium Constants, Free-Energy Differences, Changes in Free-Energy Differences, and Transition Rates for PRE^{-A} Complexes. The equilibrium constants, free-energy differences, changes in free-energy differences, and transition rates reported in Tables S2–S5 for PRE^{-A} complexes were calculated as described below. Following previously described procedures (13, 16), the first 20 time points of each idealized smFRET vs. time trajectory were used to plot a one-dimensional E_{FRET} histogram for each dataset. The analysis was restricted to the first 20 time points to avoid using any time points in which photobleaching of Cy5 while Cy3 continues to emit yields photobleaching-induced $E_{FRET} = 0$ values. Each of the two peaks that were observed in each in the one-dimensional E_{FRET} histograms was fitted to a Gaussian distribution, using Origin 7.0 (OriginLab Corporation), with initial guesses for the centers of the Gaussian distributions set at E_{FRET} values of ∼0.35 and ∼0.55 (for smFRET$_{L1–L9}$ datasets) and ∼0.15 and ∼0.75 (for smFRET$_{L1-tRNA}$ datasets), respectively. High and low E_{FRET} threshold values defining the E_{FRET} windows corresponding to L1$_o$ and L1$_c$ (in smFRET$_{L1–L9}$ datasets), or L1◦tRNA and L1•tRNA (in smFRET$_{L1-tRNA}$ datasets), were set using the equations High = C + (FWHH/2) and Low = C – (FWHH/2), where C and FWHH are the center and full width at half-height, respectively, of each Gaussian distribution.

The populations of L1$_o$ and L1$_c$ (P_{L1o} and P_{L1c}) or the populations of L1◦tRNA and L1•tRNA ($P_{L1◦tRNA}$ and $P_{L1•tRNA}$) for each dataset were then determined by counting the number of time points that fell within each E_{FRET} window in all smFRET vs. time trajectories. The fractional populations (% L1$_o$ and % L1$_c$ or % L1◦tRNA and % L1•tRNA) reported in Fig. S1C were the relative percentages of P_{L1o} and P_{L1c} or $P_{L1◦tRNA}$ and $P_{L1•tRNA}$, respectively. The equilibrium constants K_{L1} and $K_{L1-tRNA}$ were then calculated as $K_{L1} = P_{L1c}/P_{L1o}$ and $K_{L1-tRNA} = P_{L1•tRNA}/P_{L1◦tRNA}$, respectively.

The free-energy differences between L1$_o$ and L1$_c$ (ΔG_{L1}) or between L1$\circ$tRNA and L1$\bullet$tRNA ($\Delta G_{L1\text{-}tRNA}$) were calculated using the equation $\Delta G_{L1} = -RT\ln K_{L1}$ or $\Delta G_{L1\text{-}tRNA} = -RT\ln K_{L1\text{-}tRNA}$, respectively, where R is the gas constant (1.986 cal·K^{-1}·mol^{-1}) and T is room temperature (298 K).

The changes in free-energy difference between L1$_o$ and L1$_c$ ($\Delta\Delta G_{L1}$) or between L1$\circ$tRNA and L1$\bullet$tRNA ($\Delta\Delta G_{L1\text{-}tRNA}$) were calculated using the equation $\Delta\Delta G_{L1,n} = \Delta G_{L1,n} - \Delta G_{L1,x}$ or $\Delta\Delta G_{L1\text{-}tRNA,n} = \Delta G_{L1\text{-}tRNA,n} - \Delta G_{L1\text{-}tRNA,x}$, respectively, where n denotes the PRE^{-A} complex whose $\Delta\Delta G_{L1}$ or $\Delta\Delta G_{L1\text{-}tRNA}$ is being calculated and x is the PRE^{-A} complex that was used as a reference complex as specified in Tables S2 and S3.

The rates of transition between L1$_o$ and L1$_c$ ($k_{L1o\rightarrow L1c}$ and $k_{L1c\rightarrow L1o}$) or between L1$\circ$tRNA and L1$\bullet$tRNA ($k_{L1\circ tRNA\rightarrow L1\bullet tRNA}$ and $k_{L1\bullet tRNA\rightarrow L1\circ tRNA}$) were determined using survival probability analyses as previously described (13, 16). Briefly, using the E$_{FRET}$ windows corresponding to L1$_o$ and L1$_c$ as described above, the dwell times spent in L1$_o$ before transitioning to L1$_c$ and the dwell times spent in L1$_c$ before transitioning to L1$_o$ were extracted from the individual idealized smFRET trajectories that exhibited fluctuations between at least two FRET states in each dataset and were plotted as one-dimensional survival probability plots. The lifetimes of L1$_o$ (τ_{L1o}) and L1$_c$ (τ_{L1c}) were then determined by fitting the survival probability plots with single-exponential decays (13, 14, 16). Because two of the three observed subpopulations of E$_{FRET}$ trajectories for each dataset do not exhibit any fluctuations before their being truncated due to fluorophore photobleaching or, more rarely, to the finite observation time (60 s) of our experiments (Fig. S1 A and B), use of only the fluctuating subpopulation of E$_{FRET}$ trajectories to calculate transition rates using survival probability analyses, as was done here, systematically overestimates the transition rates (24). To correct for the fact that these two, prematurely truncated subpopulations of E$_{FRET}$ trajectories were not included in the survival probability analysis (i.e., because they do not exhibit any fluctuations), $k_{L1o\rightarrow L1c}$ was ultimately calculated by taking the inverse of τ_{L1o} and subtracting both the inverse of the lifetime of the fluorophore before photobleaching (measured independently as 11.1 ± 2.1 s for Cy5 in L1$_o$) and the inverse of the total observation time (13, 24, 25). $k_{L1c\rightarrow L1o}$ was calculated and corrected in an analogous manner, using τ_{L1c} and the independently measured lifetime of 9.9 ± 1.3 s for Cy5 in L1$_c$. The analogous analysis was used to obtain $k_{L1\circ tRNA\rightarrow L1\bullet tRNA}$ and $k_{L1\bullet tRNA\rightarrow L1\circ tRNA}$ from the smFRET$_{L1\text{-}tRNA}$ datasets with the exceptions that (i) the E$_{FRET}$ windows corresponding to L1$\circ$tRNA and L1$\bullet$tRNA were used to extract the dwell times spent in L1$\circ$tRNA before transitioning to L1$\bullet$tRNA and the dwell times spent in L1$\bullet$tRNA before transitioning to L1$\circ$tRNA and (ii) $k_{L1\circ tRNA\rightarrow L1\bullet tRNA}$ and $k_{L1\bullet tRNA\rightarrow L1\circ tRNA}$ were calculated and corrected using $\tau_{L1\circ tRNA}$ and the independently measured lifetime of 5.6 ± 0.4 s for Cy5 in L1$\circ$tRNA and $\tau_{L1\bullet tRNA}$ and the independently measured lifetime of 14.4 ± 1.9 s for Cy5 in L1$\bullet$tRNA, respectively (13, 25).

The mean values and SDs of the equilibrium constants, free-energy differences, changes in free-energy differences, and transition rates reported in Tables S2, S3, and S5 for PRE^{-A} complexes were calculated using three independently recorded and analyzed datasets.

13. Calculation of Equilibrium Constants, Free-Energy Differences, Changes in Free-Energy Differences, and Transition Rates for Vacant 70S Ribosomes. The K_{L1}, ΔG_{L1}, and $\Delta\Delta G_{L1}$ values reported in Tables S4 and S5 for vacant 70S ribosomes were calculated as described for PRE^{-A} complexes (*SI Materials and Methods*, section 12) with a slight modification. Because the absence of a P-site tRNA in vacant 70S ribosomes shifts the L1$_o\rightleftarrows$ L1$_c$ equilibrium dramatically toward L1$_o$ (Figs. S1C and S4A and Table S4), the relatively small peak corresponding to L1$_c$ in the one-dimensional E$_{FRET}$ histograms is "buried" underneath the rela-

tively larger peak corresponding to L1$_o$ (example in Fig. 3 of the main text). Thus, it is difficult to accurately fit the peaks corresponding to L1$_o$ and L1$_c$ to separate Gaussian distributions as described in *SI Materials and Methods*, section 12. Therefore, rather than using the centers and full widths at half-heights of fitted Gaussian distributions to directly define the high and low E$_{FRET}$ threshold values corresponding to L1$_o$ and L1$_c$ for the vacant 70S ribosome datasets, we instead indirectly estimated the high and low E$_{FRET}$ threshold values defining L1$_o$ and L1$_c$ for the vacant 70S ribosome datasets by using the average high and low E$_{FRET}$ threshold values defining L1$_o$ and L1$_c$ obtained from all of the PRE^{-A} complexes. The corresponding averages were as follows: high L1$_o$ threshold E$_{FRET}$ = 0.60, low L1$_o$ threshold E$_{FRET}$ = 0.48, high L1$_c$ threshold E$_{FRET}$ = 0.39, and low L1$_c$ threshold E$_{FRET}$ = 0.28. Using these average high and low E$_{FRET}$ threshold values corresponding to L1$_o$ and L1$_c$, K_{L1}, ΔG_{L1}, and $\Delta\Delta G_{L1}$ and their associated errors were calculated for each vacant 70S ribosome dataset as described for the PRE^{-A} datasets in *SI Materials and Methods*, section 12.

Because of the stability of L1$_o$, vacant 70S ribosomes primarily sample L1$_o$ and rarely undergo L1$_o\rightarrow$L1$_c$ transitions before photobleaching of the Cy5 fluorophore. As a consequence, vacant 70S ribosomes seldom sample L1$_c$ and only infrequently undergo L1$_c\rightarrow$L1$_o$ transitions. This makes it very difficult to extract a statistically relevant number of dwell times spent in L1$_o$ before transitioning to L1$_c$ and dwell times spent in L1$_c$ before transitioning to L1$_o$ from the individual idealized smFRET trajectories of vacant 70S ribosomes, thereby limiting the accuracy with which the survival probability analysis method described in *SI Materials and Methods*, section 12 can be used to determine τ_{L1o} and τ_{L1c} and, consequently, $k_{L1o\rightarrow L1c}$ and $k_{L1c\rightarrow L1o}$. Because of this limitation of the survival probability analysis method described in *SI Materials and Methods*, section 12, we have instead used a transition probability matrix approach (26) to determine $k_{L1o\rightarrow L1c}$ and $k_{L1c\rightarrow L1o}$ for vacant 70S ribosomes (Table S4). Briefly, the average high and low E$_{FRET}$ threshold values defining L1$_o$ and L1$_c$ that were obtained from all of the PRE^{-A} complexes as described in the previous paragraph were first applied to each idealized smFRET trajectory to assign each time point before photobleaching in each idealized smFRET trajectory to either L1$_o$ (0.48 ≤ E$_{FRET}$ ≤ 0.60) or L1$_c$ (0.28 ≤ E$_{FRET}$ ≤ 0.39). Next, a 2 × 2 counting matrix was constructed using the thresholded, idealized smFRET trajectories,

$$\text{Counting Matrix} = C = \begin{bmatrix} c_{L1o\rightarrow L1o} & c_{L1o\rightarrow L1c} \\ c_{L1c\rightarrow L1o} & c_{L1c\rightarrow L1c} \end{bmatrix},$$

where the matrix element c_{ij} denotes the total number of times the smFRET signal is observed to be in state i at time t and state j at time $t + \Delta t$, where Δt corresponds to 0.1 s, in the entire set of idealized smFRET vs. time trajectories recorded for each vacant 70S ribosome. A transition probability matrix was then generated by row normalization of the counting matrix, $a_{ij} = c_{ij}/\Sigma_j c_{ij}$, resulting in a set of transition probabilities that sum to 1 for each state row i:

$$\text{Transition Probability Matrix} = A = \begin{bmatrix} a_{L1o\rightarrow L1o} & a_{L1o\rightarrow L1c} \\ a_{L1c\rightarrow L1o} & a_{L1c\rightarrow L1c} \end{bmatrix}.$$

Here a_{ij} represents the probability of transitioning to the jth state at time $t + \Delta t$ when the system is in the ith state at time t. The kinetic rates, k_{ij}, are defined by a system of linear, first-order differential equations of the form

$$\frac{d\rho_i(t)}{dt} = \sum_j k_{ij}\rho_j(t),$$

where ρ_i denotes the number of molecules in the ith state at time t. The matrix of rates, K, is related to the transition probability matrix, A, via the matrix exponential:

$$A = e^{K\Delta t} = \sum_n \frac{(K\Delta t)^n}{n!}.$$

Expansion of the above relationship to first order results in

$$A = I + K\Delta t + O\left((K\Delta t)^2\right),$$

where I is the identity matrix. This allows us to define our rate matrix as

$$\text{Rate Matrix} = K = \begin{bmatrix} k_{L1o \to L1o} & k_{L1o \to L1c} \\ k_{L1c \to L1o} & k_{L1c \to L1c} \end{bmatrix}$$

$$= \begin{bmatrix} \dfrac{a_{L1o \to L1o} - 1}{\Delta t} & \dfrac{a_{L1o \to L1c}}{\Delta t} \\ \dfrac{a_{L1c \to L1o}}{\Delta t} & \dfrac{a_{L1c \to L1c} - 1}{\Delta t} \end{bmatrix}.$$

Using the rate matrix, $k_{L1o \to L1c}$ and $k_{L1c \to L1o}$ were then obtained using the equations $k_{L1o \to L1c} = a_{L1o \to L1c}/\Delta t$ and $k_{L1c \to L1o} = a_{L1c \to L1o}/\Delta t$, respectively.

1. Horovitz A (1996) Double-mutant cycles: A powerful tool for analyzing protein structure and function. *Fold Des* 1(6):121–126.
2. Cukras AR, Green R (2005) Multiple effects of S13 in modulating the strength of intersubunit interactions in the ribosome during translation. *J Mol Biol* 349(1):47–59.
3. Zhou J, Lancaster L, Trakhanov S, Noller HF (2012) Crystal structure of release factor RF3 trapped in the GTP state on a rotated conformation of the ribosome. *RNA* 18(2):230–240.
4. Jin H, Kelley AC, Ramakrishnan V (2011) Crystal structure of the hybrid state of ribosome in complex with the guanosine triphosphatase release factor 3. *Proc Natl Acad Sci USA* 108(38):15798–15803.
5. Dunkle JA, et al. (2011) Structures of the bacterial ribosome in classical and hybrid states of tRNA binding. *Science* 332(6032):981–984.
6. Atta M, et al. (2012) The methylthiolation reaction mediated by the Radical-SAM enzymes. *Biochim Biophys Acta* 1824(11):1223–1230.
7. Sievers F, et al. (2011) Fast, scalable generation of high-quality protein multiple sequence alignments using Clustal Omega. *Mol Syst Biol* 7:539.
8. Waterhouse AM, Procter JB, Martin DM, Clamp M, Barton GJ (2009) Jalview Version 2—a multiple sequence alignment editor and analysis workbench. *Bioinformatics* 25(9):1189–1191.
9. Punta M, et al. (2012) The Pfam protein families database. *Nucleic Acids Res* 40(Database issue):D290–D301.
10. Culver GM, Noller HF (2000) In vitro reconstitution of 30S ribosomal subunits using complete set of recombinant proteins. *Methods Enzymol* 318:446–460.
11. Blanchard SC, Kim HD, Gonzalez RL, Jr, Puglisi JD, Chu S (2004) tRNA dynamics on the ribosome during translation. *Proc Natl Acad Sci USA* 101(35):12893–12898.
12. Fei J, et al. (2010) A highly purified, fluorescently labeled in vitro translation system for single-molecule studies of protein synthesis. *Methods Enzymol* 472:221–259.
13. Fei J, et al. (2009) Allosteric collaboration between elongation factor G and the ribosomal L1 stalk directs tRNA movements during translation. *Proc Natl Acad Sci USA* 106(37):15702–15707.
14. Fei J, Kosuri P, MacDougall DD, Gonzalez RL, Jr (2008) Coupling of ribosomal L1 stalk and tRNA dynamics during translation elongation. *Mol Cell* 30(3):348–359.
15. Aitken CE, Marshall RA, Puglisi JD (2008) An oxygen scavenging system for improvement of dye stability in single-molecule fluorescence experiments. *Biophys J* 94(5):1826–1835.
16. Fei J, Richard AC, Bronson JE, Gonzalez RL, Jr (2011) Transfer RNA-mediated regulation of ribosome dynamics during protein synthesis. *Nat Struct Mol Biol* 18(9):1043–1051.
17. Southworth DR, Brunelle JL, Green R (2002) EFG-independent translocation of the mRNA:tRNA complex is promoted by modification of the ribosome with thiol-specific reagents. *J Mol Biol* 324(4):611–623.
18. Pestka S (1971) Inhibitors of ribosome functions. *Annu Rev Microbiol* 25:487–562.
19. Semenkov Yu, Shapkina T, Makhno V, Kirillov S (1992) Puromycin reaction for the A site-bound peptidyl-tRNA. *FEBS Lett* 296(2):207–210.
20. Kim HD, Puglisi JD, Chu S (2007) Fluctuations of transfer RNAs between classical and hybrid states. *Biophys J* 93(10):3575–3582.
21. Frank J, Gonzalez RL, Jr (2010) Structure and dynamics of a processive Brownian motor: The translating ribosome. *Annu Rev Biochem* 79:381–412.
22. Gonzalez RL, Jr, Chu S, Puglisi JD (2007) Thiostrepton inhibition of tRNA delivery to the ribosome. *RNA* 13(12):2091–2097.
23. Bronson JE, Fei J, Hofman JM, Gonzalez RL, Jr, Wiggins CH (2009) Learning rates and states from biophysical time series: A Bayesian approach to model selection and single-molecule FRET data. *Biophys J* 97(12):3196–3205.
24. Bartley LE, Zhuang X, Das R, Chu S, Herschlag D (2003) Exploration of the transition state for tertiary structure formation between an RNA helix and a large structured RNA. *J Mol Biol* 328(5):1011–1026.
25. Sternberg SH, Fei J, Prywes N, McGrath KA, Gonzalez RL, Jr (2009) Translation factors direct intrinsic ribosome dynamics during translation termination and ribosome recycling. *Nat Struct Mol Biol* 16(8):861–868.
26. Greenfeld M, Pavlichin DS, Mabuchi H, Herschlag D (2012) Single Molecule Analysis Research Tool (SMART): An integrated approach for analyzing single molecule data. *PLoS ONE* 7(2):e30024.
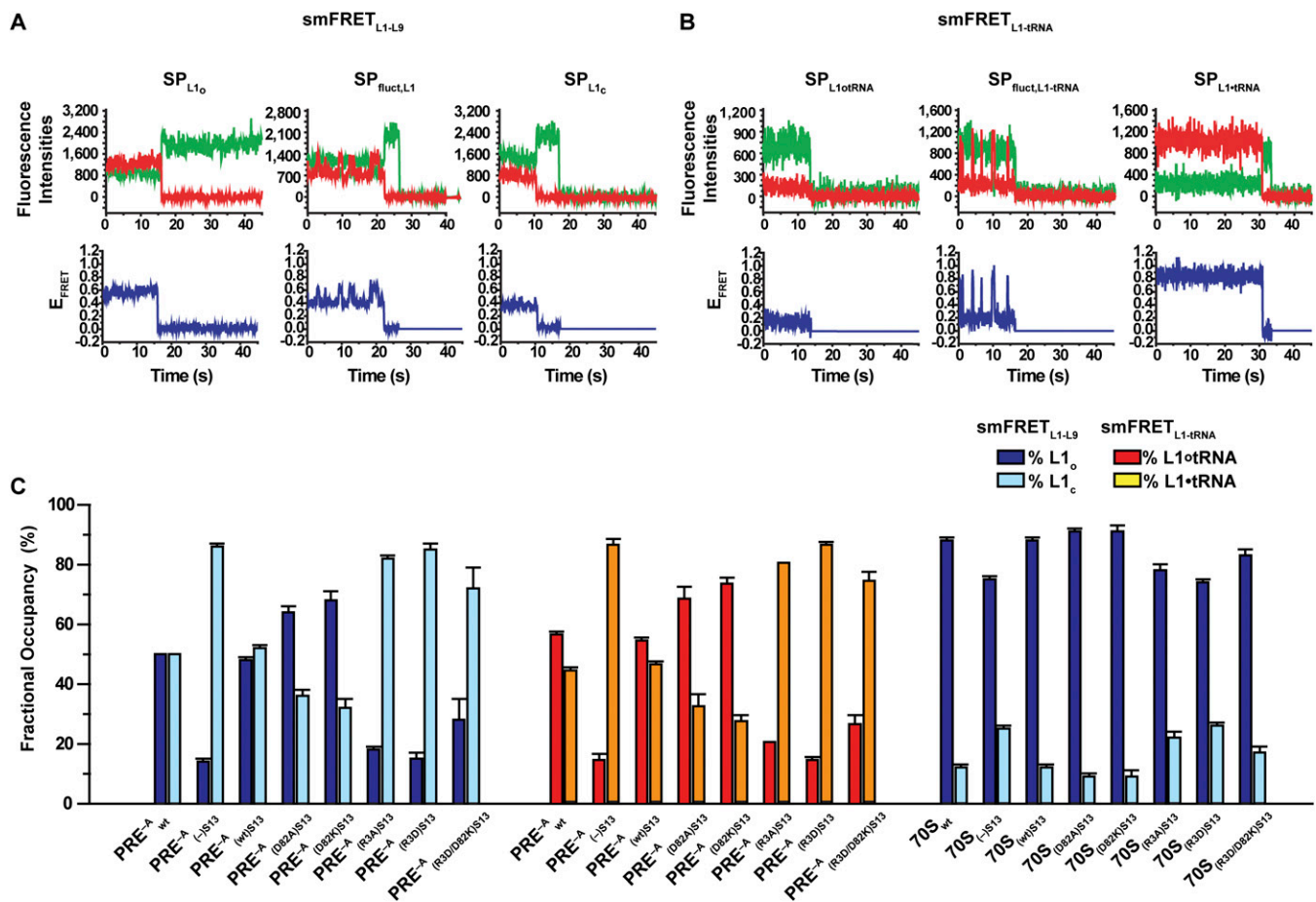
Fig. S1. Sample FRET efficiency (E_{FRET}) vs. time trajectories and the fractional occupancies of $L1_o$ and $L1_c$ or L1∘tRNA and L1•tRNA for each PRE^{-A} complex and vacant 70S ribosome. (*A*) Sample E_{FRET} vs. time trajectories using the $smFRET_{L1-L9}$ signal. (*Upper*) Representative Cy3 (green) and Cy5 (red) emission intensity vs. time trajectories are shown. (*Lower*) The corresponding E_{FRET} (blue) vs. time trajectories were calculated using $E_{FRET} = I_{Cy5}/(I_{Cy3} + I_{Cy5})$, where E_{FRET} is the FRET efficiency at each time point and I_{Cy3} and I_{Cy5} are the Cy3 and Cy5 emission intensities, respectively. Three subpopulations of E_{FRET} trajectories were observed: SP_{L1_o} (*Left*) exhibits a stable FRET state centered at 0.56 ± 0.02; $SP_{fluct,L1}$ (*Center*) exhibits fluctuations between two FRET states centered at 0.56 ± 0.02 and 0.35 ± 0.01; and SP_{L1_c} (*Right*) exhibits a stable FRET state centered at 0.35 ± 0.01. (*B*) Sample E_{FRET} vs. time trajectories using the $smFRET_{L1-tRNA}$ signal. Representative Cy3 and Cy5 emission intensity vs. time trajectories and the corresponding E_{FRET} vs. time trajectories are displayed as in *A*. Three subpopulations of E_{FRET} trajectories were observed: $SP_{L1∘tRNA}$ (*Left*) exhibits a stable FRET state centered at 0.15 ± 0.02; $SP_{fluct,L1-tRNA}$ (*Center*) exhibits fluctuations between two FRET states centered at 0.15 ± 0.02 and 0.74 ± 0.03; and $SP_{L1•tRNA}$ (*Right*) exhibits a stable FRET state centered at 0.74 ± 0.03. (*C*) Bar graphs of the fractional occupancies of $L1_o$ and $L1_c$ (% $L1_o$ and % $L1_c$) or L1∘tRNA and L1•tRNA (% L1∘tRNA and % L1•tRNA) for each PRE^{-A} complex and vacant 70S ribosome calculated as described in *SI Materials and Methods*. Data are presented as the mean $\pm$ SD of three independent measurements.
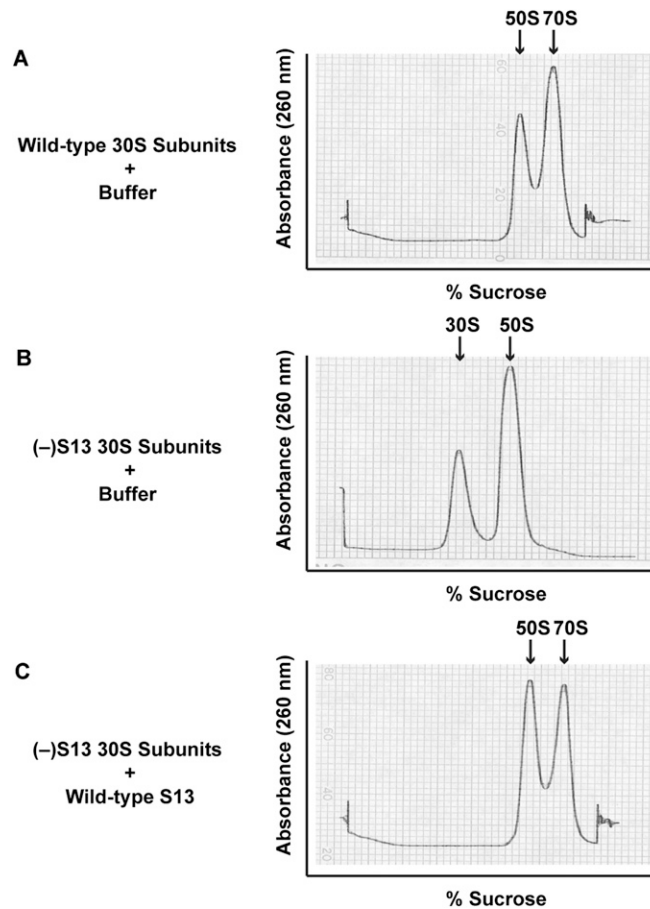
Fig. S2. Purification of S13-reconsitituted 30S subunits away from (−)S13 30S subunits, using a subunit association-based purification protocol. The 50S subunits were added to (−)S13 30S subunits that had been preincubated with purified recombinant wild-type S13 or S13 mutant under conditions in which only S13-reconstituted 30S subunits can form 70S ribosomes. The 70S ribosomes containing S13-reconstituted 30S subunits were subsequently purified using sucrose gradient (further details in *SI Materials and Methods*). (*A*) The 50S subunits added to wild-type 30S subunits preincubated in buffer are shown as a positive control. (*B*) The 50S subunits added to (−)S13 30S subunits preincubated in buffer are shown as a negative control. (*C*) The 50S subunits added to (−)S13 30S subunits preincubated with purified recombinant wild-type S13 are shown as an example; 30S subunits reconstituted with each S13 mutant were purified in an analogous manner.
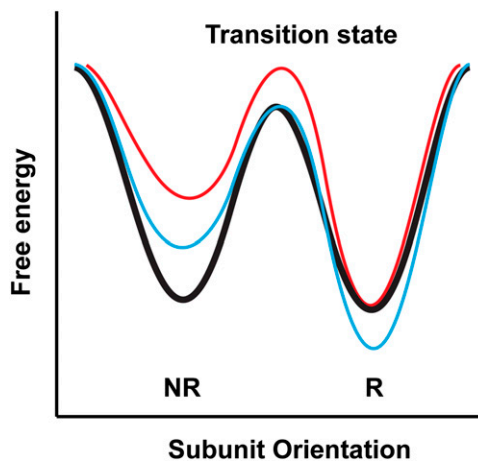
Fig. S3. Interpretation of the small, but detectable and reproducible, decreases in $k_{L1c \to L1o}$ and $k_{L1 \bullet tRNA \to L1 \circ tRNA}$ caused by (R3)S13 mutations. For maximum clarity, the free-energy landscape governing the intersubunit dynamics of $PRE_{(WT(S13))}^{-A}$ is depicted as a simplified, one-dimensional schematic (black curve). There are at least two possible origins of the small decreases in $k_{L1c \to L1o}$ and $k_{L1 \bullet tRNA \to L1 \circ tRNA}$ caused by (R3)S13 mutations. The first possibility is that these small effects arise from an (R3)S13 mutation-mediated increase in the stability of the R-subunit orientation of the PRE^{-A} complexes (blue curve). Although within the R-subunit orientation, (R3)S13 is too far away from any negatively charged residues within the 50S subunit to form salt bridges (structural analysis described in Fig. 1 of the main text), it is nonetheless likely that (R3)S13 participates in a network of relatively weaker, longer-distance, electrostatic interactions with other charged residues within the PRE^{-A} complex. Given such a scenario, mutations to (R3)S13 could potentially alter this network in such a way to stabilize the R-subunit orientation of the PRE^{-A} complex, thus providing a plausible explanation for the small decreases in $k_{L1c \to L1o}$ and $k_{L1 \bullet tRNA \to L1 \circ tRNA}$ that we observe in $PRE_{(R3A)S13}^{-A}$ and $PRE_{(R3D)S13}^{-A}$. The second possibility is that our mutations to (R3)S13 alter the stability of one or more of the transition-state subunit orientations that are sampled during R→NR transitions in a manner that slightly increases the overall free-energy barrier that must be overcome for PRE/PRE^{-A} complexes to undergo R→NR transitions (red curve).
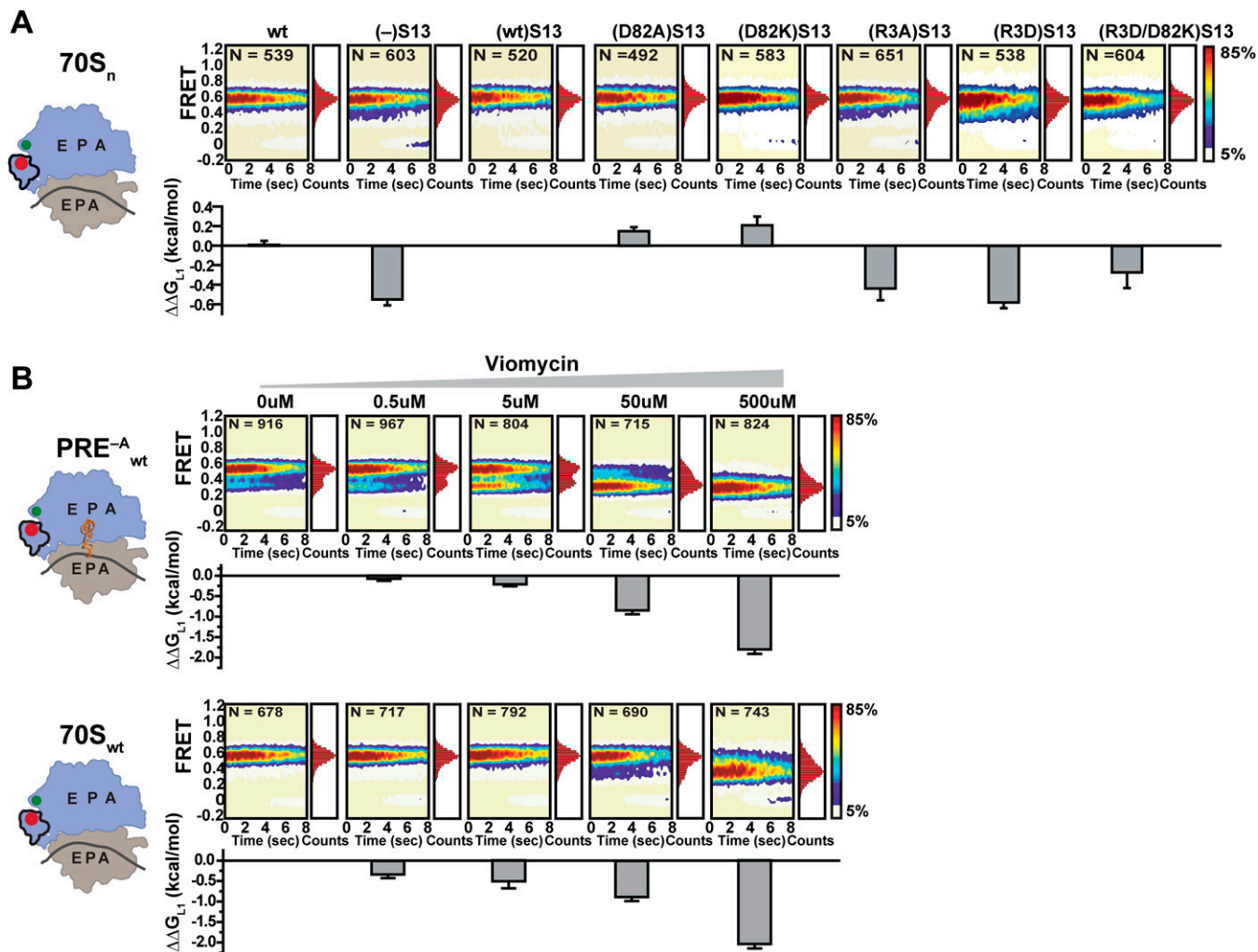
Fig. S4. Coupling of L1-stalk dynamics and intersubunit rotation in the absence of P-site tRNA. (*A*) Steady-state smFRET measurements and changes in the free-energy differences of vacant 70S ribosomes formed using WT, (−)S13, (WT)S13, (D82A)S13, (D82K)S13, (R3A)S13, (R3D)S13, and (R3D/D82K)S13 30S subunits using the $smFRET_{L1-L9}$ signal. Data are displayed as in Fig. 2 of the main text, with the exception that the changes in the free-energy difference depicted in the bar graphs are given relative to $70S_{(WT)S13}$ and were generated using the $\Delta\Delta G_{L1}$ values calculated and reported in Table S4. (*B*) Steady-state smFRET measurements and changes in the free-energy differences of PRE_{WT}^{-A} (*Upper*) and $70S_{WT}$ (*Lower*) as a function of increasing viomycin concentration, using the $smFRET_{L1-L9}$ signal. Data are displayed as in Fig. 2 of the main text, with the exception that the changes in the free energy difference for each viomycin concentration depicted in the bar graphs are given relative to the 0-μM viomycin condition and were generated using the $\Delta\Delta G_{L1}$ values calculated and reported in Table S5.
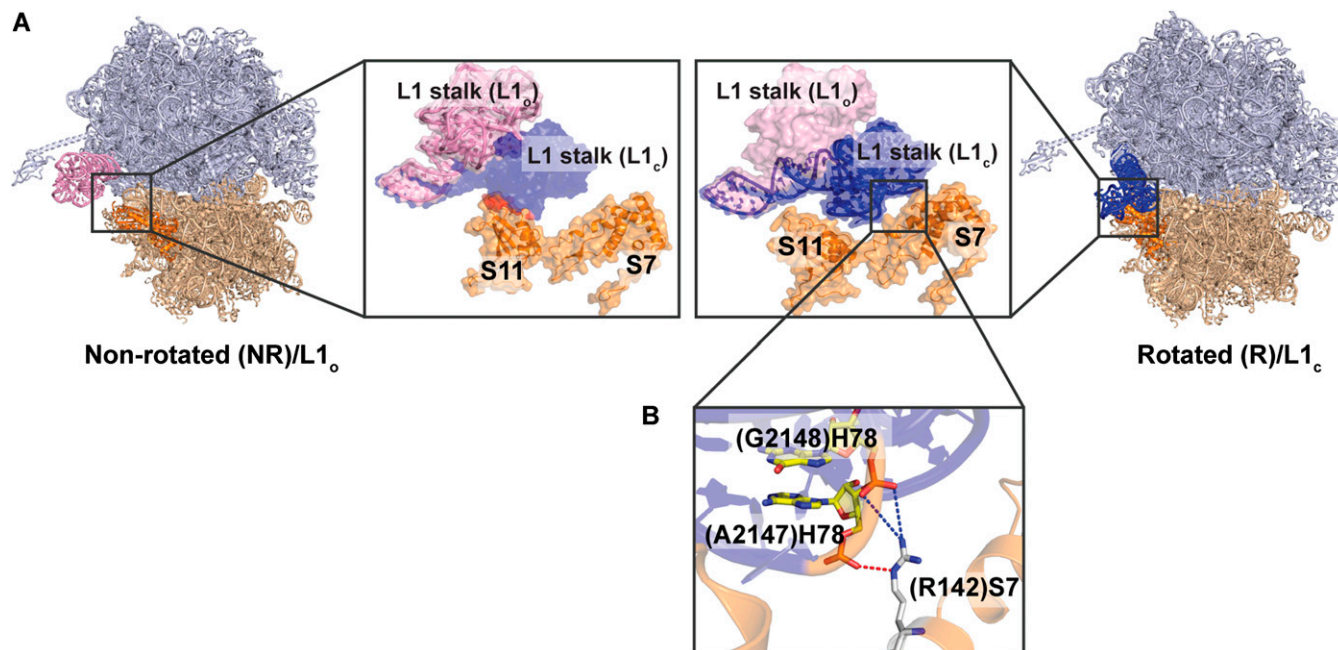
Fig. S5. L1-stalk–S7/S11 interactions in ribosomal complexes that are in the NR- and R-subunit orientations. (*A*) The structure of a ribosomal complex containing a ribosome in the NR-subunit orientation (*Left*) (PDB IDs: 3R8S and 3R8T) and a ribosomal complex containing a ribosome in the R-subunit orientation (*Right*) (PDB IDs: 3R8N and 3R8O). (*Left*) The zoomed-in view demonstrates that the $L1_c$ conformation of the L1 stalk (dark-blue, semitransparent, space-filling/cartoon representation) would sterically clash (red) with S11 (orange space-filling/cartoon representation) within a ribosome that is in the NR-subunit orientation; such a clash would likely preclude the L1 stalk from stably adopting the $L1_c$ conformation within the context of the NR-subunit orientation, thereby favoring the $L1_o$ conformation of the L1 stalk (pink space-filling/cartoon representation). (*Right*) The zoomed-in view demonstrates that the $L1_c$ conformation of the L1 stalk (dark-blue space-filling/cartoon representation) can dock into a pocket that is formed within the platform region of the 30S subunit and make favorable electrostatic and van der Waals packing interactions with ribosomal proteins S7 (orange space-filling/cartoon representation) and S11; such interactions likely help to stabilize the $L1_c$ conformation of the L1 stalk within the context of the R-subunit orientation and thus disfavor the $L1_o$ conformation of the L1 stalk (pink, semitransparent, space-filling/cartoon representation). (*Left*) The zoomed-in view was generated by incorporating the structure of a ribosomal complex containing a ribosome in the R-subunit orientation into the structure of the ribosomal complex containing a ribosome in the NR-subunit orientation and aligning the 23S rRNA (excluding H76–78) of the ribosome in the NR-subunit orientation (chain A in PDB ID 3R8T) with the 23S rRNA (excluding H76–78) of the ribosome in the R-subunit orientation (chain A in PDB ID 3R8O), using PyMol (1). (*Right*) Likewise, the zoomed-in view was generated by incorporating the structure of a ribosomal complex containing a ribosome in the NR-subunit orientation into the structure of the ribosomal complex containing a ribosome in the R-subunit orientation and aligning the 23S rRNA (excluding H76–78) of the ribosome in the NR-subunit orientation (chain A in PDB ID 3R8O) with the 23S rRNA (excluding H76–78) of the ribosome in the R-subunit orientation (chain A in PDB ID 3R8T), using PyMol. For clarity, ribosome structural elements other than L1, H76–78, S7, and S11 are not shown in the zoomed-in views. (*B*) Close-up view of the hydrogen bonding interaction (red dashed line) and electrostatic interactions (blue dashed lines) that are formed between adenine 2147 and guanine 2148 in the 23S rRNA H78 component of the L1 stalk [(A2147)H78 and (G2148)H78] and arginine 142 of ribosomal protein S7 [(R142)S7]. (A2147)H78, (G2148)H78, and (R142)S7 are labeled, colored by atom, and depicted in stick representations. The hydrogen bonding interaction was characterized by a distance of 2.91 Å between the side-chain nitrogen atom of (R142)S7 and the backbone oxygen atom of (A2147)H78. Electrostatic interactions were characterized by distances of 4.03 Å and 4.32 Å between the side-chain nitrogen atom of (R142)S7 and the two backbone oxygen atoms of (G2148)H78, respectively.

1. Schrodinger L (2010) *The PyMOL Molecular Graphics System*, Version 1.3r1.
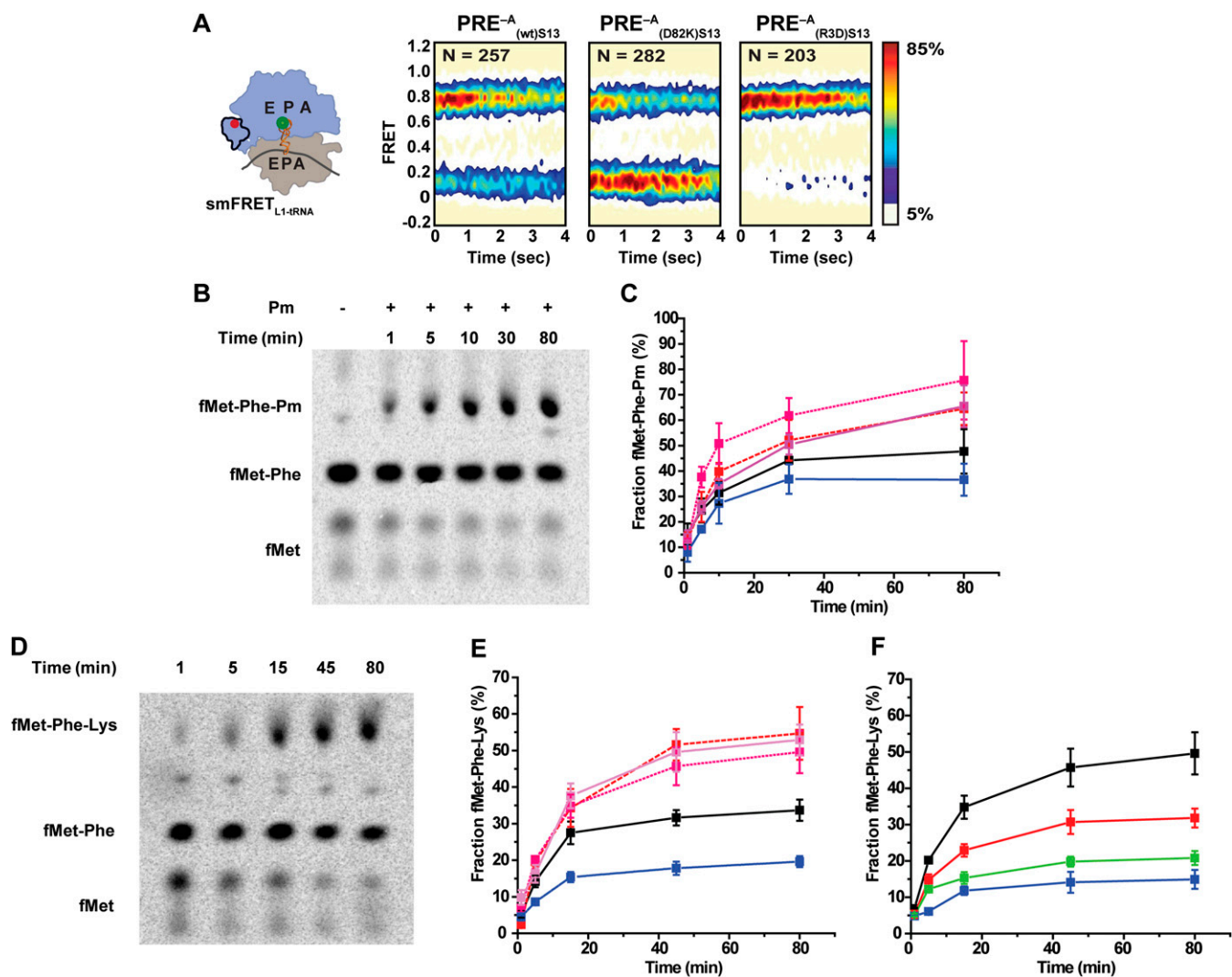
Fig. S6. Assessing the propensity of PRE complexes to undergo EF-G–independent translocation, using a puromycin reactivity assay and a tripeptide synthesis assay. (*A*) The effect of buffer conditions on the L1•tRNA⇌L1∘tRNA equilibrium. smFRET$_{L1\text{-tRNA}}$ experiments on three PRE^{-A} complexes [PRE$^{-A}_{(WT)S13}$, PRE$^{-A}_{(D82K)S13}$, and PRE$^{-A}_{(R3D)S13}$] were repeated using the same buffer conditions that were used for the puromycin reactivity assays (i.e., translocation buffer containing 8 mM Mg^{2+}) rather than in the Tris-Polymix buffer containing 15 mM Mg^{2+} in which all of the other smFRET$_{L1\text{-tRNA}}$ experiments reported in this article were performed (*SI Materials and Methods*). The results of these control smFRET$_{L1\text{-tRNA}}$ experiments demonstrate that the effects of the D82K and R3D S13 mutations on the L1∘tRNA⇌L1•tRNA equilibrium are the same in the two buffer systems, namely that, relative to PRE$^{-A}_{(WT)S13}$, PRE$^{-A}_{(D82K)S13}$ exhibits a shift of the L1∘tRNA⇌L1•tRNA equilibrium toward L1∘tRNA and PRE$^{-A}_{(R3D)S13}$ exhibits a shift of the L1∘tRNA⇌L1•tRNA equilibrium toward L1•tRNA (compare Fig. 2 *C*, *E*, and *G* of the main text with *A*, *Left*, *Center*, and *Right*, respectively). (*B*) A representative electrophoretic TLC (eTLC) plate showing the formation of fMet–Phe–Pm (where Pm denotes puromycin) in the absence of EF-G over time in translocation buffer containing 8 mM MgCl$_2$ (*SI Materials and Methods*). (*C*) Analysis of the rate and extent of EF-G–independent translocation using the puromycin synthesis assay demonstrates that all of the PRE complexes that exhibit conformational equilibria that are shifted toward R/L1$_o$/(P/E) relative to PRE$_{(WT)S13}$ (black) [i.e., PRE$_{(-)S13}$ (red), PRE$_{(R3D)S13}$ (magenta), and PRE$_{(R3D/D82K)S13}$ (purple)] display a corresponding increase in the rate and extent of EF-G–independent translocation relative to PRE$_{(WT)S13}$. In contrast, the PRE complex that exhibits conformational equilibria that are shifted toward NR/L1$_o$/(P/P) relative to PRE$_{(WT)S13}$ [i.e., PRE$_{(D82K)S13}$ (blue)] displays a corresponding decrease in the rate and extent of EF-G–independent translocation relative to PRE$_{(WT)S13}$. (*D*) A representative eTLC plate showing the formation of fMet–Phe–Lys in the absence of EF-G over time in translocation buffer containing 8 mM MgCl$_2$ (*SI Materials and Methods*). (*E*) Consistent with the analysis of the rate and extent of EF-G–independent translocation using the puromycin reactivity assays in *A* and *B*, analysis of the rate and extent of EF-G–independent translocation using the tripeptide synthesis assay demonstrates that PRE$_{(-)S13}$ (red), PRE$_{(R3D)S13}$ (magenta), and PRE$_{(R3D/D82K)S13}$ (purple) all exhibit an increase in the rate and extent of EF-G–independent translocation relative to PRE$_{(WT)S13}$ (black) whereas PRE$_{(D82K)S13}$ (blue) exhibits a decrease in the rate and extent of EF-G–independent translocation relative to PRE$_{(WT)S13}$. (*F*) The effect of Mg^{2+} concentration on the rate and extent of EF-G–independent translocation was analyzed using the tripeptide synthesis assay described in *D* and *E* and a representative PRE complex, PRE$_{(R3D)S13}$. Tripeptide synthesis reactions performed in translocation buffer containing 8 mM Mg^{2+} (black), 10 mM Mg^{2+} (red), 12 mM Mg^{2+} (green), and 15 mM Mg^{2+} (blue) demonstrate that increasing the Mg^{2+} concentration of the translocation buffer, which shifts the conformational equilibria of the PRE complex toward L1$_o$ and L1∘tRNA (20, 21), decreases the rate and extent of EF-G–independent translocation.

Table S1. Phylogenetic analyses of ribosomal proteins S7, S13, and L5

Ribosomal proteins	Amino acids*	PID (%)[†]	
		Prokaryotes only[‡]	Prokaryotes and eukaryotes[§]
S7	R142	54 (99)[¶]	59 (90)[‖]
S13	R3	99	77
	D82	63 (86)**	42 (71)[††]
L5	R111	85	81
	D112	91	83
	D143	97	93

*R, arginine; K, lysine; D, aspartic acid; E, glutamic acid.
[†]PID, percentage of identity.
[‡]The sequence alignment was performed using 971 fully sequenced eubacterial and archaebacterial genomes (*SI Materials and Methods*).
[§]The sequence alignment was performed using 3,000–5,000 prokaryotic and eukaryotic protein sequences acquired from Pfam (*SI Materials and Methods*).
[¶]PID of positively charged residues at position (142)S7 is 99% (R, 54%; K, 45%).
[‖]PID of positively charged residues at position (142)S7 is 90% (R, 59%; K, 31%).
**PID of negatively charged residues at position (82)S13 is 86% (D, 63%; E, 23%).
[††]PID of negatively charged residues at position (82)S13 is 71% (D, 42%; E, 29%).

Table S2. Equilibrium constants, free-energy differences, changes in free-energy differences, and transition rates for PRE^{-A} complexes formed using different 30S subunits: smFRET$_{L1\text{-}tRNA}$

PRE$_n^{-A}$	$K_{L1\text{-}tRNA}$	$\Delta G_{L1\text{-}tRNA}$, kcal·mol^{-1}	$\Delta\Delta G_{L1\text{-}tRNA}$, kcal·mol^{-1}	$k_{L1\circ tRNA\rightarrow L1\bullet tRNA}$, s^{-1}	$k_{L1\bullet tRNA\rightarrow L1\circ tRNA}$, s^{-1}	Normalized $k_{L1\circ tRNA\rightarrow L1\bullet tRNA}$	Normalized $k_{L1\bullet tRNA\rightarrow L1\circ tRNA}$
WT	**0.83 ± 0.04**	**-0.11 ± 0.04**	**0**	**0.91 ± 0.21**	**0.69 ± 0.10**	**1.00 ± 0.23**	**1.00 ± 0.14**
(−)S13	5.92 ± 1.64	−1.04 ± 0.16	−0.93. ± 0.21	5.23 ± 0.65	0.49 ± 0.14	5.75. ± 0.71	0.71 ± 0.20
(WT)S13	0.83 ± 0.10	0.12 ± 0.07	0.01 ± 0.06	1.15 ± 0.07	0.97 ± 0.09	1.26 ± 0.08	1.40 ± 0.13
(WT)S13	**0.83 ± 0.10**	**0.12 ± 0.07**	**0**	**1.15 ± 0.07**	**0.97 ± 0.09**	**1.00 ± 0.06**	**1.00 ± 0.09**
(D82A)S13	0.46 ± 0.06	0.47 ± 0.08	0.36 ± 0.15	1.10 ± 0.15	1.86 ± 0.23	0.95 ± 0.13	1.92 ± 0.23
(D82K)S13	0.39 ± 0.05	0.57 ± 0.08	0.45 ± 0.11	1.06 ± 0.14	2.22 ± 0.30	0.92 ± 0.12	2.29 ± 0.31
(R3A)S13	3.92 + 0.50	−0.81 ± 0.08	−0.93 ± 0.14	2.85 ± 0.74	0.65 ± 0.15	2.48 ± 0.65	0.67 ± 0.15
(R3D)S13	5.70 ± 1.39	−1.02 ± 0.14	−1.14 ± 0.21	6.34 ± 0.64	0.60 ± 0.15	5.51 ± 0.56	0.62 ± 0.15
(R3D/D82K)S13	2.84 ± 0.87	−0.59 ± 0.21	−0.71 ± 0.28	4.81 ± 1.76	2.02 ± 0.59	4.18 ± 1.55	2.08 ± 0.61

Mean ± SD of equilibrium constants, free-energy differences, changes in free-energy differences, and transition rates for each PRE^{-A} complex were calculated as described in *SI Materials and Methods* from three independent datasets. ΔΔGs and normalized transition rates for PRE$_{(-)S13}^{-A}$ and PRE$_{(WT)S13}^{-A}$ were calculated relative to PRE$_{WT}^{-A}$ (shown in boldface type). ΔΔGs and normalized transition rates for each PRE^{-A} complex carrying an S13-reconstituted 30S subunit were calculated relative to PRE$_{(WT)S13}^{-A}$ (shown in boldface type).

Table S3. Equilibrium constants, free-energy differences, changes in free-energy differences, and transition rates for PRE^{-A} complexes formed using different 30S subunits: smFRET$_{L1-L9}$

PRE$_n^{-A}$	K_{L1}	ΔG_{L1}, kcal·mol^{-1}	$\Delta\Delta G_{L1}$, kcal·mol^{-1}	$k_{L1o\rightarrow L1c}$, s^{-1}	$k_{L1c\rightarrow L1o}$, s^{-1}	Normalized $k_{L1o\rightarrow L1c}$	Normalized $k_{L1c\rightarrow L1o}$
WT	**0.97 ± 0.06**	**0.02 ± 0.04**	**0**	**0.65 ± 0.14**	**0.76 ± 0.05**	**1.00 ± 0.21**	**1.00 ± 0.07**
(−)S13	6.16 ± 1.22	−1.07 ± 0.13	−1.09 ± 0.11	4.90 ± 1.88	0.51 ± 0.19	7.53 ± 2.73	0.67 ± 0.25
(WT)S13	1.15 ± 0.11	−0.08 ± 0.06	−0.10 ± 0.09	0.87 ± 0.17	1.00 ± 0.10	1.26 ± 0.26	1.31 ± 0.13
(WT)S13	**1.15 ± 0.11**	**-0.08 ± 0.06**	**0**	**0.87 ± 0.17**	**1.00 ± 0.10**	**1.00 ± 0.19**	**1.00 ± 0.10**
(D82A)S13	0.52 ± 0.10	0.40 ± 0.12	0.48 ± 0.13	1.02 ± 0.12	1.88 ± 0.41	1.17 ± 0.13	1.88 ± 0.41
(D82K)S13	0.38 ± 0.04	0.58 ± 0.06	0.66 ± 0.05	0.78 ± 0.12	2.04 ± 0.30	0.89 ± 0.13	2.04 ± 0.30
(R3A)S13	4.41 ± 0.45	−0.88 ± 0.06	−0.80 ± 0.10	1.79 ± 0.36	0.82 ± 0.16	2.06 ± 0.41	0.82 ± 0.16
(R3D)S13	6.06 ± 0.37	−1.07 ± 0.04	−0.99 ± 0.05	3.12 ± 0.66	0.71 ± 0.07	3.59 ± 0.75	0.71 ± 0.07
(R3D/D82K)S13	1.97 ± 0.44	−0.64 ± 0.09	−0.56 ± 0.07	2.57 ± 0.48	1.76 ± 0.41	2.95 ± 0.55	1.76 ± 0.41

Data are displayed as in Table S2.

Table S4. Equilibrium constants, free-energy differences, changes in free-energy differences, and transition rates for vacant 70S ribosomes formed using different 30S subunits: smFRET$_{L1-L9}$

70S$_n$	K_{L1}	ΔG_{L1}, kcal·mol^{-1}	$\Delta\Delta G_{L1}$, kcal·mol^{-1}	$k_{L1o\to L1c}$, s^{-1}	$k_{L1c\to L1o}$, s^{-1}	Normalized $k_{L1o\to L1c}$	Normalized $k_{L1c\to L1o}$
WT	0.13 ± 0.01	1.20 ± 0.04	0.00 ± 0.04	0.03 ± 0.01	0.17 ± 0.04	1.08 ± 0.40	0.78 ± 0.18
(–)S13	0.33 ± 0.02	0.66 ± 0.02	−0.55 ± 0.06	0.08 ± 0.02	0.15 ± 0.02	2.67 ± 0.72	0.68 ± 0.10
(WT)S13	**0.13 ± 0.02**	**1.21 ± 0.08**	**0**	**0.03 ± 0.00**	**0.22 ± 0.03**	**1.00 ± 0.16**	**1.00 ± 0.13**
(D82A)S13	0.10 ± 0.01	1.36 ± 0.07	0.15 ± 0.04	0.03 ± 0.02	0.28 ± 0.04	1.09 ± 0.57	1.29 ± 0.19
(D82K)S13	0.10 ± 0.02	1.41 ± 0.15	0.21 ± 0.09	0.03 ± 0.01	0.30 ± 0.11	0.94 ± 0.18	1.38 ± 0.50
(R3A)S13	0.28 ± 0.03	0.76 ± 0.06	−0.44 ± 0.12	0.04 ± 0.01	0.20 ± 0.03	1.35 ± 0.23	0.90 ± 0.15
(R3D)S13	0.35 ± 0.03	0.63 ± 0.05	−0.58 ± 0.06	0.07 ± 0.03	0.20 ± 0.06	2.15 ± 0.90	0.90 ± 0.26
(R3D/D82K)S13	0.21 ± 0.03	0.94 ± 0.08	−0.27 ± 0.16	0.04 ± 0.02	0.26 ± 0.09	1.39 ± 0.76	1.22 ± 0.41

Data are displayed as in Table S2, with the exception that $\Delta\Delta G$s and normalized transition rates for each vacant 70S ribosome were calculated relative to 70S$_{(WT)S13}$ (shown in boldface type).

Table S5. Equilibrium constants, free-energy differences, and changes in free-energy differences for PRE$_{WT}^{-A}$ and 70S$_{WT}$ as a function of viomycin concentration

Viomycin, μM	PRE$_{WT}^{-A}$			70S$_{WT}$		
	K_{L1}	ΔG_{L1}, kcal·mol^{-1}	$\Delta\Delta G_{L1}$, kcal·mol^{-1}	K_{L1}	ΔG_{L1}, kcal·mol^{-1}	$\Delta\Delta G_{L1}$, kcal·mol^{-1}
0	**0.50 ± 0.01**	**0.41 ± 0.01**	**0**	**0.08 ± 0.01**	**1.55 ± 0.04**	**0**
0.5	0.57 ± 0.04	0.34 ± 0.04	−0.08 ± 0.05	0.13 ± 0.01	1.22 ± 0.05	−0.33 ± 0.09
5	0.72 ± 0.07	0.20 ± 0.06	−0.21 ± 0.05	0.18 ± 0.04	1.04 ± 0.13	−0.51 ± 0.17
50	2.09 ± 0.30	−0.43 ± 0.09	−0.85 ± 0.09	0.34 ± 0.08	0.67 ± 0.14	−0.88 ± 0.10
500	10.4 ± 1.9	−1.39 ± 0.11	−1.80 ± 0.11	2.28 ± 0.25	−0.49 ± 0.07	−2.04 ± 0.11

Data are displayed as in Tables S2–S4, with the exception that $\Delta\Delta G$s were calculated relative to the 0-μM viomycin condition (shown in boldface type).